 doi:10.20944/preprints202206.0249.v1

Article

Validation of the Cooling Model for TMCP Processing of Steel Sheets with Oxide Scale by Industrial Experiment Data

Emmanuil Beygelzimer [1]* and Yan Beygelzimer [2]

[1] OMD-engineering LLC, Dnipro, Ukraine; markbeygelzimer@omd-engineering.com
[2] Donetsk Institute for Physics and Engineering named after A.A. Galkin, National Academy of Sciences of Ukraine, Kyiv, Ukraine; yanbeygel@gmail.com
* Correspondence: emmanuilomd@gmail.com; Tel.: +380503686342

Abstract: To verify the authors' mathematical model for water jet cooling of steel sheet, the previously performed experimental studies of temperature of the test plate in the roller quenching machine (RQM) were used. The calculated data of steel temperature evolution along the RQM length were compared with the readings of thermocouples inserted in the center of the test plate and at its surfaces. The core of the model is the dependence of the temperatures of film, transition and nucleate boiling regimes on the thickness of the oxide scale layer on the cooled surface. It was found that the model correctly takes into account the oxide scale on the sheet surface, flow rates and combinations of the RQM banks used, water temperature and other factors. For all experiments the calculated metal temperature corresponds well to the measured one. In the experiments with interrupted cooling, the calculated temperature plots repeat the characteristic changes in the experimental curves. The main uncertainty in the modeling of cooling in a wide temperature range can be contributed by the random nature of changes in the oxide scale thickness during water cooling. In this regard, the estimated thickness of the oxide scale layer should be considered as the main parameter for adapting the sheet temperature control process. The obtained data confirm the possibility of effective application of the model in the ACS of industrial TMCP (Thermo-Mechanical Controlled Process) systems.

Keywords: rolled flat products; accelerated cooling; temperature; mathematical model; oxide scale; Thermo-Mechanical Controlled Process

1. Introduction

The recent development of the global rolled steel market is characterized by a constant increase in the share of products obtained by means of the Thermo-Mechanical Controlled Process (TMCP) [1, 2]. The essence of this process is the combination of controlled hot rolling with controlled cooling in the temperature range of microstructural transformations in steel [3]. Potentially TMCP has the possibility to contribute rolled products such a combination of properties (e.g., strength, ductility, toughness, cold resistance, weldability, etc.) that is not available with other techniques [4-7]. This peculiarity is due to the special mechanism of formation of the fine-grained steel microstructure during phase transformations under conditions of rapid cooling in combination with the deformed structure of the initial phase [3, 8]. It is extremely difficult to achieve such a microstructure by other technological solutions (for instance, by microalloying) without controlled cooling. Moreover, in-line equipment for controlled cooling make it possible to increase the efficiency of other technical and technological tools for imparting the required set of properties to the finished rolled products, including microalloying [9].

In practice, however, realizing the benefits of TMCP faces the problems of ensuring precise control and uniformity of temperature and cooling rate as well as flatness of the TMCP-products [10]. When steel products are cooled with water, the biggest problems occur when accelerated cooling to temperatures below about 550 °C. This is due to the fact

Preprints (www.preprints.org) | NOT PEER-REVIEWED | Posted: 17 June 2022 doi:10.20944/preprints202206.0249.v1

that during cooling to such average mass temperatures there is a sharp increase in cooling intensity due to the transition from film to nucleate regime of water boiling on the steel surface [11] (p.424). The surface temperature at which this transition begins (often referred to as the Leidenfrost temperature) lies in the wide range, as a rule from 300 to 800 °C, depending on a number of non-deterministic factors [12], and therefore can only be predicted with a fairly large error. In industrial mills, the problem is exacerbated by the presence of oxide scale on the steel surface, since the thickness and properties of this scale have a very strong influence on the Leidenfrost temperature and heat transfer in general [13-18]. Therefore, the adequacy of the mathematical model of accelerated cooling in the presence of oxide scale on the cooled surface is decisive for the effective design and management of the TMCP process.

Several mathematical models used in various installations for accelerated cooling of rolled steel are known from open sources [19-25]. However, these models do not take into account the thickness and properties of oxide scale on the surface of the cooled metal. Given these circumstances, the authors of this article have been developing their own mathematical model of the temperature evolution of steel plates in a water-cooling unit of arbitrary configuration since the early 2000s. To date, the authors' model has been used in automated control systems on five industrial water-cooling units, including the 1700 hot strip mill, 2800 and 3000 plate mills, and roller quenching machines [26-28].

The principal novelty of the latest version of the authors' model is that it explicitly takes into account the thickness and thermophysical properties of the oxide scale on the cooled surface. The **goal** of this work is to compare the calculations by the authors' model with reliable temperature measurements during water cooling of sheets with oxide scale over a wide temperature range covering the different boiling regimes.

2. Materials and Methods

2.1. Cooling model

The authors' model implements numerical calculation of the temperature in the sheet as it moves along the cooling unit. Six different types of cooling zones are distinguished (Figure 1): 1) jet impingement, 2) supercritical parallel water flow on the top surface, 3) subcritical parallel water flow on the top surface, 4) parallel water flow on the bottom surface, 5) contact with a roll and 6) air cooling. Calculation of heat transfer coefficient in each zone is performed by physically meaningful (not statistical) equations. This makes it possible to take into account all the main physical factors determining the cooling process: type of jets (circular or flat, compact or spray), speed of water upon impingement and spreading on the sheet, regimes of water boiling on the surface, thickness of oxide scale, dependence of thermophysical properties of steel, scale and water on temperature, etc.

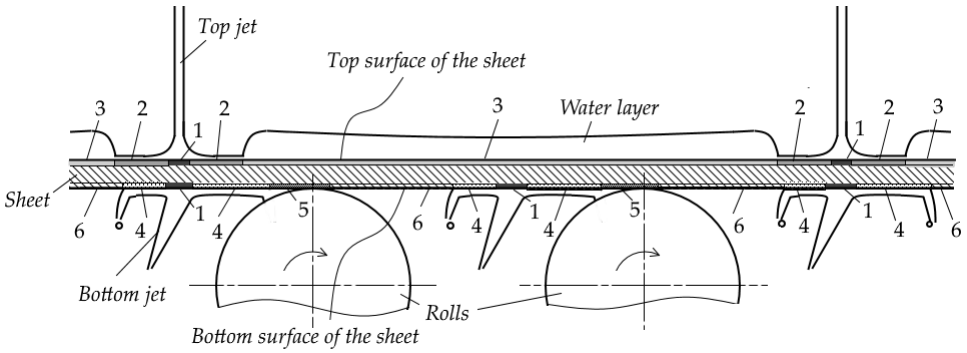

Figure 1. Schematic explaining the types of cooling zones considered in the model (indicated by numbers): 1 – jet impingement; 2 – supercritical flow on the top surface; 3 – subcritical flow on the top surface; 4 – parallel flow on the bottom surface; 5 – contact with a roll; 6 – air cooling.

Preprints (www.preprints.org) | NOT PEER-REVIEWED | Posted: 17 June 2022 doi:10.20944/preprints202206.0249.v1

Since the model is intended mainly for use in automated real-time TMCP control systems, the authors preferred simple engineering methods that exclude repetitive lengthy calculations. That is why, in many cases, the authors were forced to find their own solutions, which, under specific conditions, produce results close to the rigorous but more time-consuming procedures. In other words, the authors followed such an approach to mathematical modeling, which involves not developing as detailed a model as possible with its subsequent numerical solution, but selecting the main physical parameters that affect the process, and building a model that allows a simple analytical solution (the application of such an approach is described, for example, in [29, 30]).

The block diagram of the model is shown in Figure 2. Below is a brief description of the original authors' methods for calculating the key parameters. Known methods of other authors, used in the model under consideration, are given without description, only with appropriate references.

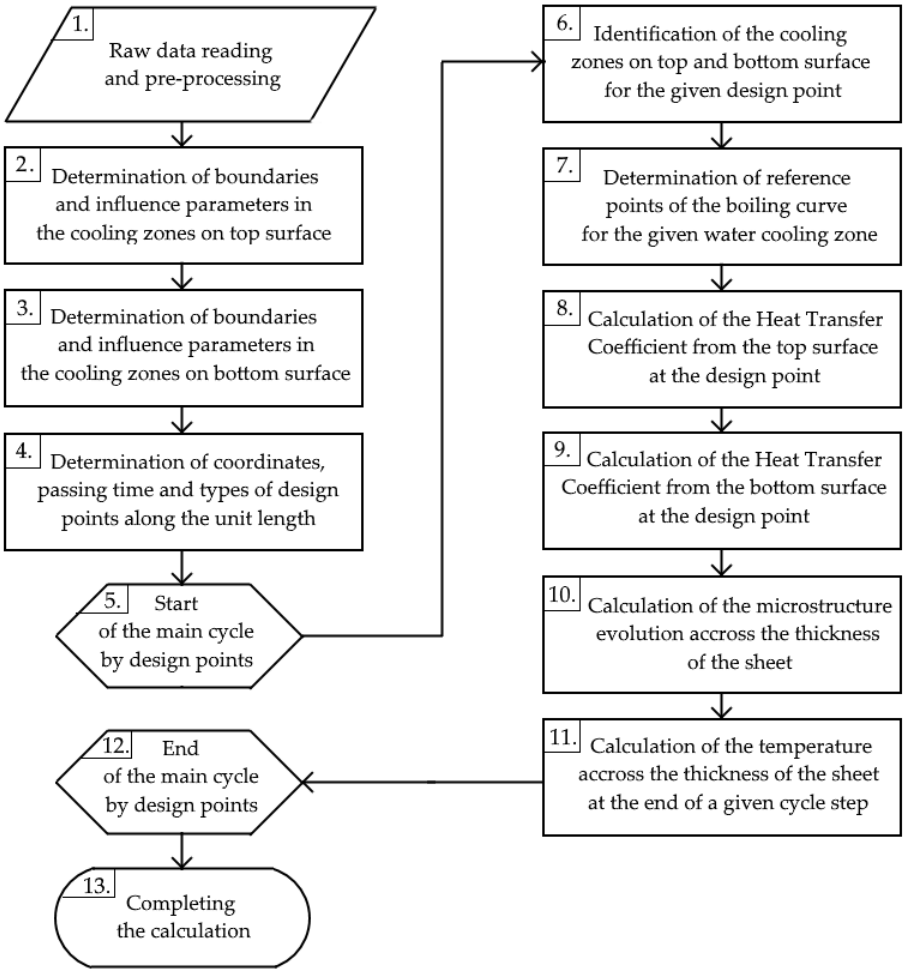

Figure 2. Block diagram of the cooling model

2.1.1. Boundaries of water cooling zones and parameters of water flow[1]

To determine the boundaries of an impingement zone produced by a spray jet (Figure 3), the authors obtained the following formula for the *arbitrary radius of the impact spot* by methods of analytical geometry [31]:

[1]Used in blocks 2 and 3 of the diagram in Figure 2.

Preprints (www.preprints.org) | NOT PEER-REVIEWED | Posted: 17 June 2022 doi:10.20944/preprints202206.0249.v1

$$R_\theta = \left(r_\theta + \frac{H}{\cos\gamma}\operatorname{tg}\varphi\right)\frac{\sqrt{1+(\sin\theta\,\operatorname{tg}\gamma)^2}}{1-\sin\theta\,\operatorname{tg}\gamma\,\operatorname{tg}\varphi} \quad (1)$$

where θ is a polar angle of the given radius as the angle between this radius and the polar axis of the nozzle[2]; r_θ is the nozzle outlet radius [m] with polar angle θ; R_θ is the impact spot radius as the length of the central projection of the given nozzle outlet radius I on the sheet plane [m]; H is the distance from the center of the nozzle outlet to the sheet plane [m]; γ is an inclination angle as the angle between the longitudinal axis of the jet and the normal to the sheet plane; φ is an open angle as the angle between the given generatrix of the spray cone and its longitudinal axis.

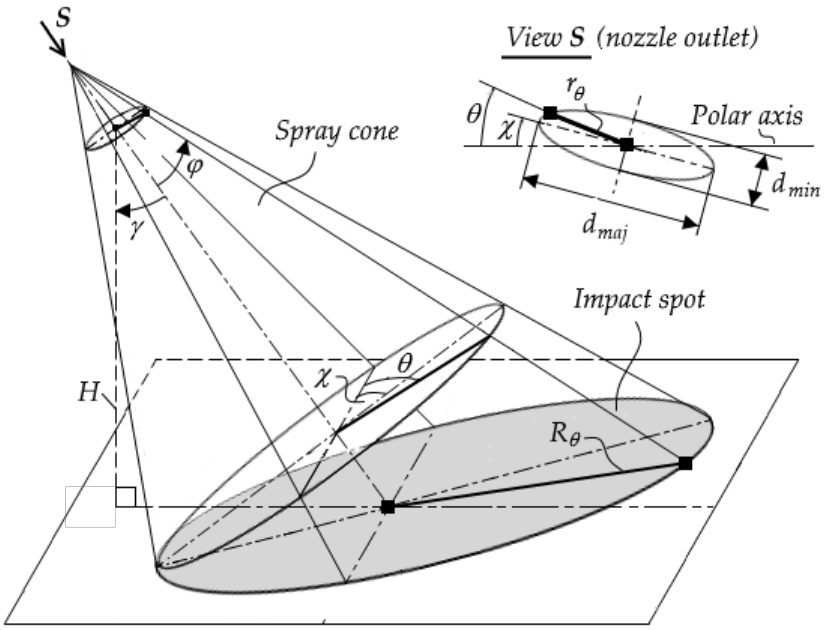

Figure 3. Schematic explaining the designations used in calculating the dimensions of the impact spot of the spray jet.

Based on formula (1), the *area of the impact spot A* [m²] is calculated as follows:

$$A = \frac{\pi}{4}\left(d_{\text{maj}} + \frac{2H}{\cos\gamma}\operatorname{tg}\varphi_{\text{maj}}\right)\left(d_{\text{min}} + \frac{2H}{\cos\gamma}\operatorname{tg}\varphi_{\text{min}}\right)k_{\text{maj}}k_{\text{min}} \quad (2)$$

where

$$k_{\text{maj}} = \frac{\sqrt{1+(\sin\chi\,\operatorname{tg}\gamma)^2}}{1-\left(\sin\chi\,\operatorname{tg}\gamma\,\operatorname{tg}\varphi_{\text{maj}}\right)^2} \quad (3)$$

$$k_{\text{min}} = \frac{\sqrt{1+(\cos\chi\,\operatorname{tg}\gamma)^2}}{1-(\cos\chi\,\operatorname{tg}\gamma\,\operatorname{tg}\varphi_{\text{min}})^2} \quad (4)$$

d_{maj} and d_{min} are the major and the minor diameters of the nozzle outlet, respectively; φ_{maj} and φ_{min} are the open angles at the major and minor diameters of the nozzle outlet, respectively; χ is a nozzle rotation angle as the angle between the polar axis and the major diameter of the nozzle outlet.

[2]The polar axis is parallel to the plane of the sheet and in most cases is aligned with the longitudinal axis of the collector with nozzles.

Preprints (www.preprints.org) | NOT PEER-REVIEWED | Posted: 17 June 2022 doi:10.20944/preprints202206.0249.v1

Compared to the known solution [32], formula (2) takes into account the rotation of the nozzle around its longitudinal axis and the dimensions of the nozzle outlet orifice. In the actual conditions of accelerated cooling systems, these factors can increase the impact area of the spray jet by up to 30%.

To calculate the *speed of spray drops in the impingement zone* the authors derived the approximate analytical solution of the differential equation of drop motion in the field of gravity taking into account the resistance of the vapor-gas medium [33]. The key assumptions are the constancy of inclination angle, drag coefficient and radius of the drop along its trajectory. These assumptions are valid for operating conditions of spray nozzles for accelerated cooling and quenching of metal sheets, namely: drop diameter $d = 0.5 \cdot 10^{-3} \ldots 3.0 \cdot 10^{-3}$ m, distance from the nozzle outlet to the cooled surface $H = 0.1 \ldots 1.0$ m, angle of the drop departure the nozzle relative to the horizontal $\beta_0 = 30 \ldots 90°$, speed of the drop when departure the nozzle $u_0 = 10 \ldots 40$ m·s^{-1}, Reynolds number $\mathrm{Re} = u_0 d/\nu_a \approx 10^3 \ldots 10^4$ (ν_a is the kinematic viscosity of the vapor-gas medium [m^2·s^{-1}]). The final formula for the drop speed is as follows:

$$u = u_0 \exp(-k_u HS) \sqrt{1 \pm g \frac{\exp(2k_u HS) - 1}{u_0^2 k_u S}} \tag{5}$$

where the "+" sign under the square root refers to the drop going downward (i.e., for the top jet), and the "-" sign refers to the drop going upward (i.e., for the bottom jet); u is the speed of the water drop when impinging on the sheet surface [m·s^{-1}]; u_0 is the speed of the water drop as it leaves the nozzle [m·s^{-1}]; k_u is the dimensionless speed parameter of the model (see below); H is the distance from the nozzle outlet to the sheet plane [m]; g is gravitational acceleration [m·s^{-2}]; S is the complex parameter with the unit of [m^{-1}]:

$$S = \frac{3c\rho_a}{4d\rho} \tag{6}$$

c is the drag coefficient of the drop moving in a vapor-air medium (according to data from [34] (p. 694) for sphere when $Re = 10^3 \ldots 10^4$, can be taken c = 0.45); d is the diameter of the drop [m]; ρ and ρ_a are the density of the drop and the medium respectively [kg·m^{-3}].

The analytical expressions for the speed parameter of the model k_u are obtained by adaptation to the results of numerical integration of the differential equation of the motion for the top and the bottom drops separately:

– for the drops going downward:

$$\left.\begin{aligned} k_u &= \frac{1}{\sin\beta_0}, && \text{when } \frac{H\sqrt{gS}}{u_0 \sin\beta_0} \le 0.17 \\ k_u &= \frac{1}{6}\left(1 + \frac{5}{\sin\beta_0}\right), && \text{when } \frac{H\sqrt{gS}}{u_0 \sin\beta_0} > 0.17 \end{aligned}\right\} \tag{7}$$

– for the drops going upward:

$$k_u = \frac{1}{\sin\beta_0} \tag{8}$$

where β_0 is the angle of the drop departure the nozzle relative to the horizontal, for the axis of the spray jet this angle is related to the jet inclination angle (see Figure 3) as $\beta_0 = \pi/2 - \gamma$.

The model allows to calculate the *dimensions of the supercritical water flow zone* on the top surface (i.e. before the start of the hydraulic jump) for both circular and flat jets.

The supercritical flow zone from the *circular jet*, is simplistically divided into two regions: inviscid and viscous flow (Figure 4), with the assumption of constant water height in the viscous flow region. Based on these simplifications, solving the differential equation of gradually varied flow in an open segmental channel with no slope [35] (p. 119) together with the ordinary hydraulic jump equation [36] (p. 653) leads to the following results [37].

Preprints (www.preprints.org) | NOT PEER-REVIEWED | Posted: 17 June 2022 doi:10.20944/preprints202206.0249.v1

- The boundary post-jump height, above which the jump becomes submerged [m]:

$$h_{2\text{sub}} = \sqrt{\frac{a^2}{64} + \frac{V^2}{2g\pi^2 a^3}} - \frac{a}{8} \tag{9}$$

- The boundary post-jump height, above which the jump occurs inside the inviscid flow region [m]:

$$h_{2\text{vis}} = \sqrt{\frac{h_1^2}{4} + \frac{2V^2 h_1}{g\pi^2 a^4}} - \frac{h_1}{2} \tag{10}$$

where V is the jet flow [$m^3 \cdot s^{-1}$]; a is the radius of the undisturbed jet before impinging on the surface [m]; g is gravitational acceleration [$m \cdot s^{-2}$]; h_2 is the height of the water layer after the jump (post-jump height) [m]; h_1 is the height of the water layer before the jump (pre-jump height) in case jump occurs inside the viscous flow region [m]:

$$h_1 = 200 n^{1,69} a \tag{11}$$

n is the roughness coefficient between water flow and sheet surface (for the considered conditions n values are between about 0.007 and 0.020 depending on the laminar or turbulent flow mode, the roughness of the sheet surface and the phase state of the water; constants in formula (11) are obtained by approximation of the numerical solution of the differential equation for the flow height);

- *Radius R_s of the circular hydraulic jump* [m] (subscript "s" from "spot"):

a) if $h_2 \le h_{2\text{vis}}$ (jump occurs inside the viscous region), then

$$R_s = \frac{V\sqrt{2}}{\pi}\left[gh_2^3\left(\left(\frac{2h_1}{h_2}+1\right)^2 - 1\right)\right]^{-\frac{1}{2}} \tag{12}$$

b) if $h_{2\text{vis}} < h_2 \le h_{2\text{sub}}$ (jump occurs inside the inviscid region), then[3]

$$R_s = \frac{V^2}{g\pi^2 h_2^2 a^2} - \frac{a^2}{2h_2} \tag{13}$$

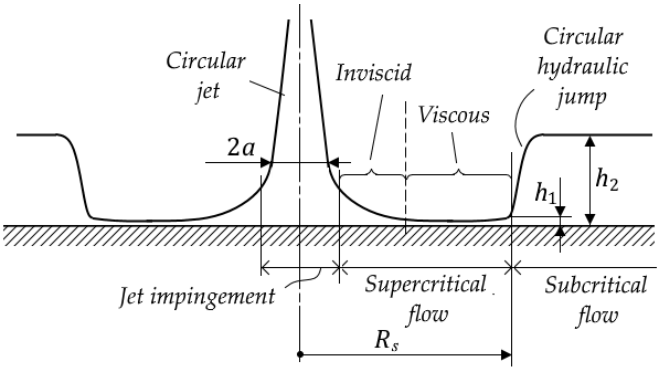

Figure 4. Schematic of the flow of a circular liquid jet on a horizontal plate with the formation of a circular hydraulic jump. The zones of jet impingement, supercritical and subcritical flow are shown. Supercritical flow zone is conventionally divided into two regions: inviscid and viscous.

In contrast to the known formulas [38], the above model allows to calculate the circular jump radius without iterative procedures.

In order to obtain a simple engineering estimate of the location of a hydraulic jump in a *plane-parallel* flow (Figure 5), the authors proposed to approximate the exponent y in the well-known Pavlovsky formula for the Chezy coefficient [40] (p. 91):

[3]expression (13) is known as the Rayleigh formula for an ideal fluid [38].

Preprints (www.preprints.org) | NOT PEER-REVIEWED | Posted: 17 June 2022 doi:10.20944/preprints202206.0249.v1

$$C = \frac{1}{n}h^y \tag{14}$$

where C is the Chezy coefficient [$m^{1/2}s^{-1}$]; n is the roughness coefficient (the physical meaning is the same as in formula (11)); h is the liquid flow height [m]; y is the exponent that in original form depends on roughness coefficient n and flow height h. Under conditions typical for industrial accelerated cooling systems ($h = 10^{-3}...10^{-1}$ m; $n = 0.007...0.02$) the function $y = y(n, h)$ with an error of no more than 6% can be approximated by the function of only one variable – the roughness coefficient [41]:

$$y = 4.5n^{0.78} \tag{15}$$

Taking according to (15) the exponent y independent of the flow height h, the differential equation of gradually varied flow in an open wide rectangular channel with no slope can be solved in explicit form [41]:

$$L_s = \frac{1}{n^2}\left[\frac{\alpha}{g(1+2y)}\left(h_1^{1+2y} - h_0^{1+2y}\right) - \frac{1}{Q_f^2(4+2y)}\left(h_1^{4+2y} - h_0^{4+2y}\right)\right] \tag{16}$$

where L_s is *the length of the supercritical zone* as the distance from the border of the jet impact zone to the hydraulic jump toe [m]; $\alpha \approx 1{,}05$ is the kinetic energy correction factor; Q_f is the specific flow rate per unit width [$m^2 \cdot s^{-1}$]; h_0 is an entry flow height as a height at the border of the jet impingement zone [m]; h_1 is the pre-jump height [m], which is related to the post-jump height by the known ratio [40] (p. 251):

$$h_1 = \frac{h_2}{2}\left(\sqrt{1 + \frac{8Q_f^2}{gh_2^3}} - 1\right) \tag{17}$$

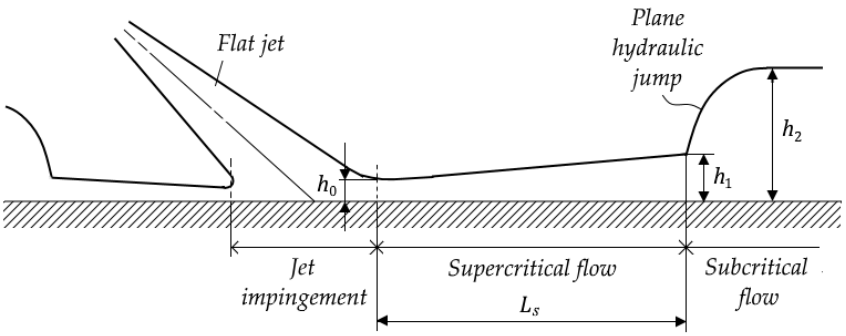

Figure 5. Schematic of the flow of a flat liquid jet on a horizontal plate with the formation of a plane hydraulic jump. The zones of jet impingement, supercritical and subcritical flow are shown.

The model considers four types of the *subcritical flow zone*, i.e. zone that lays beyond the hydraulic jump (Figure 6):

a) "*clamped layer*" – water layer between closely spaced jets on a limited area of the surface. The height of such a layer may be so great that the jets are no longer able to overcome it (the hydraulic jump becomes submerged);
b) *"bounded layer"* – water layer between adjacent rows of jets or between a row of jets and a pinch roll separated by a relatively large distance;
c) *"open layer"* – water layer, that spreads over the surface of the sheet without any obstruction; such a layer is formed, as a rule, before the first or after the last cooling bank in the absence of special devices for removing water from the surface;
d) *"shifted layer"* – water layer, which is removed from the sheet by special devices (hydro or pneumatic separators).

Preprints (www.preprints.org) | NOT PEER-REVIEWED | Posted: 17 June 2022 doi:10.20944/preprints202206.0249.v1

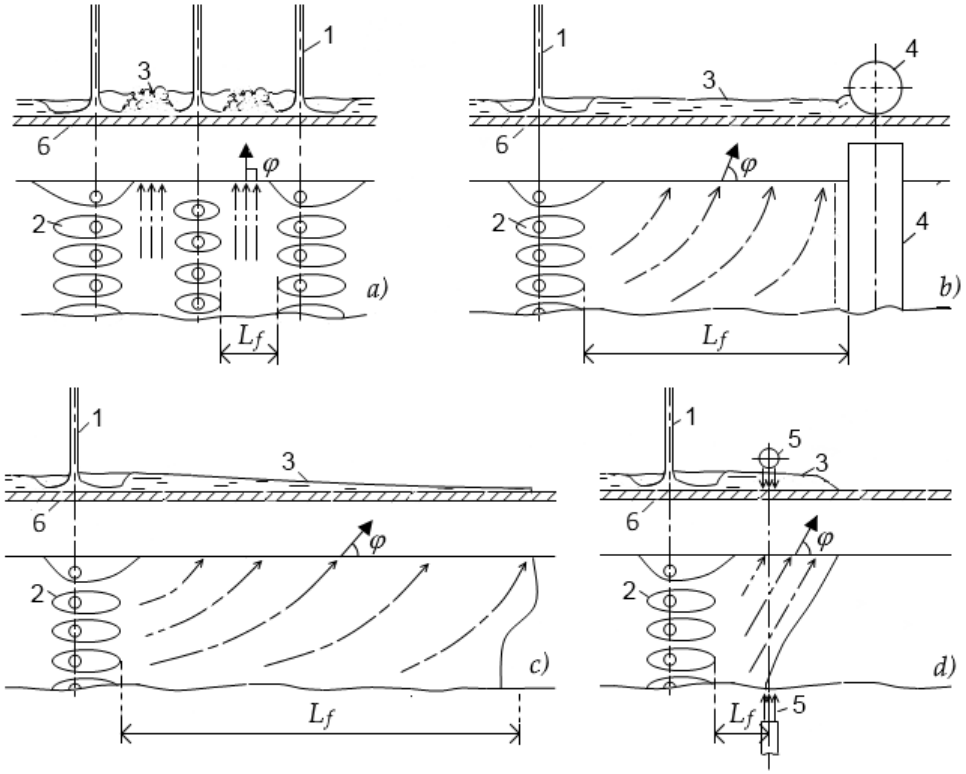

Figure 6. Different types of the subcritical flow zone ("water layer"): a) clamped, b) bounded, c) open, d) shifted. Designations: 1 – jet, 2 – supercritical flow area, 3 – water layer, 4 – roll, 5 – separator. L_f is the length of the water layer; φ is the runoff angle.

For each above type of water layer, the model calculates the height and the velocity of the flow, and for the open layer type, in addition, the length of the subcritical zone L_f [42, 43]. The method developed is based on dividing the water layer into three regions (Figure 7): direct flow, oblique flow, and stagnation. Assuming that the water flow varies gradually, the equations of motion are solved for the median streamline in the direct and oblique flow regions. As a boundary condition in the oblique flow region, the equality to unity of the Froude number on the lateral edge of the sheet is assumed (as on the weir threshold [44] (p. 391)).

In the direct flow region, continuity of the layer height at the border with the oblique flow region, is assumed as a boundary condition. At the same time, the discontinuity of velocity at this border is allowed.

As a result, the authors have proposed a procedure that allows to calculate the height and speed of water layer at all reference points of the subcritical flow zone. The key parameter of this procedure is the "angular runoff coefficient" k_φ, which means the sinus of the runoff angle, i.e. $k_\varphi \equiv \sin\varphi$.

For bounded layer the calculation of k_φ is performed using a chain of formulas:

– auxiliary parameter Φ:

$$\Phi = n^{4/3}\left[g^{2(4+2y)}\left(\frac{2L_f}{Q_f}\right)^{4(1+2y)}\right]^{1/9} \quad (18)$$

where n is the roughness coefficient (the physical meaning is the same as in formula (11)); g is gravitational acceleration [m·s^{-2}]; Q_f is the specific flow rate per unit width [m^2·s^{-1}]; L_f is the length of the subcritical zone [m]; y is the exponent (15);

– friction parameter Ω_Φ:

$$\Omega_\Phi = (1{,}05 + 0{,}43\Phi)^{3/2} \quad (19)$$

Preprints (www.preprints.org) | NOT PEER-REVIEWED | Posted: 17 June 2022 doi:10.20944/preprints202206.0249.v1

– shape parameter δ:

$$\delta = \frac{2L_f}{B_p} \tag{20}$$

– angular runoff coefficient

$$k_\varphi = \left(\frac{\Omega_\Phi}{\delta}\right)^x \tag{21}$$

where B_p is the width of the sheet [m]; $x = 0{,}5$ when $\Omega_\Phi/\delta < 1$ and $x = 0$ when $\Omega_\Phi/\delta \geq 1$.

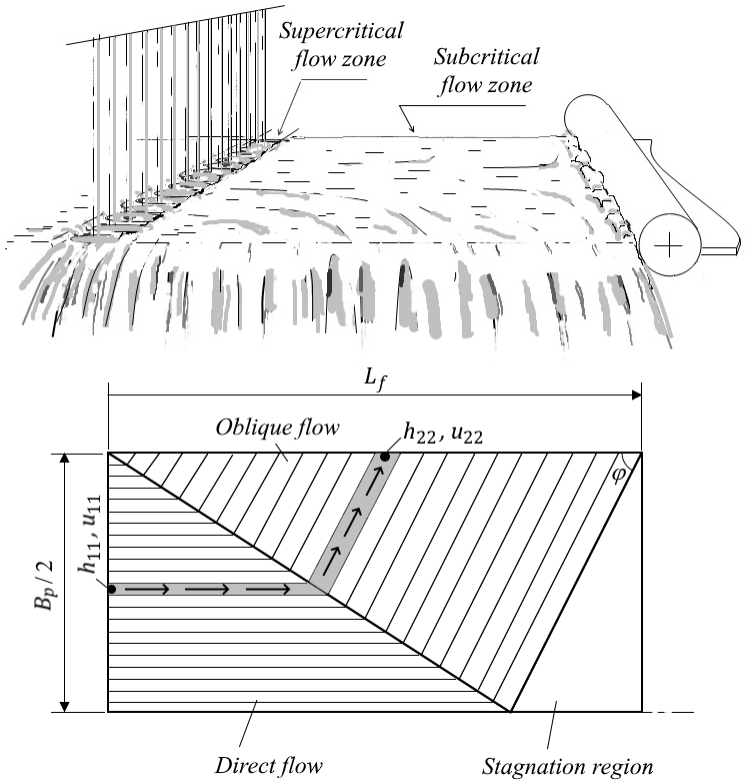

Figure 7. Schematic explaining the basic idea of calculating the parameters of the subcritical water flow zone by conventionally dividing this zone into three regions: direct flow, oblique flow and stagnation one. The arrows show the direction of water flow in the median streamline. The designations are in the text.

With a known value of k_φ, the height and speed of the flow at all key points of the water layer are calculated. For example,

$$h_{22} = \left(\frac{Q_f B_p}{2k_\varphi L_f \sqrt{g}}\right)^{\frac{2}{3}} \tag{22}$$

$$u_{22} = \sqrt{g h_{22}} \tag{23}$$

where u_{22} and h_{22} are the speed [m·s^{-1}] and the height [m] of the water at the lateral edge respectively (expression (23) follows from the equality of the Froude number to unity);

To calculate *the length of the subcritical flow zone* L_f in case of the open water layer the iteration procedure is realized. The essence of this procedure consists in solving, with respect to the desired length L_f, the system of algebraic equations obtained for the bounded layer (with the angular flow coefficient according to (21)), together with the following equation obtained for the open layer:

$$V_{fs} = k_m m_s' L_f \sqrt{2g} \left(h_{11} + \frac{u_{11}}{2g}\right)^{3/2} \tag{24}$$

Preprints (www.preprints.org) | NOT PEER-REVIEWED | Posted: 17 June 2022 doi:10.20944/preprints202206.0249.v1

where V_{fs} is the volume of water that runoffs from one lateral edge of the sheet per unit time [m^3·s^{-1}]; k_m = 0.15…0.35 is the model parameter; h_{11} and u_{11} are the height [m] and the speed [m·s^{-1}] of the water at the beginning of the subcritical zone respectively; m'_s is the lateral spillway discharge coefficient [45]:

$$m'_s = 0.45 - 0.22\frac{u_{11}^2}{gh_{11}} \quad (25)$$

2.1.2. Heat Flux in the water cooling zones[4]

Calculation of heat flux in water cooling zones at any surface temperature is performed using the concept of reference points of the boiling curve [46], which allows to avoid breaking of solutions at critical points of boiling regime change. According to this concept, on a boiling curve [47, 48], i.e. on the graph of the dependence of the heat flux on the surface temperature, in general case, six reference points of different boiling regimes are distinguished (Figure 8):

DFB - Departure of Film Boiling;
EFB - End of Film Boiling (= start of transient boiling);
DTB - Departure of Transient Boiling;
ETB - End of Transient Boiling (= start of nucleate boiling);
DNB - Departure of Nucleate Boiling;
ENB - End of Nucleate Boiling (= start of single-phase convection).

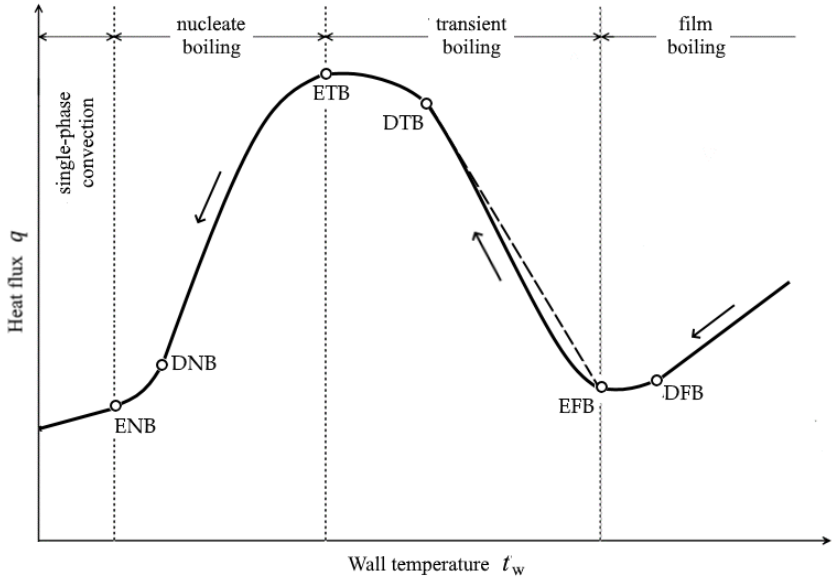

Figure 8. General view of the boiling curve. The deciphering of the reference points is given in the text. Arrows show the direction of parameter changes during cooling.

The heat flux at any surface temperature is calculated by linear interpolation between the reference points of the boiling curve. For example, if the current surface temperature refers to the transient boiling section, the heat flux is calculated as follows (the interpolation straight line for this section is shown in Figure 8):

$$q(t_w) = q_{\mathrm{DTB}} + (t_w - t_{\mathrm{DTB}})\frac{q_{\mathrm{EFB}} - q_{\mathrm{DTB}}}{t_{\mathrm{EFB}} - t_{\mathrm{DTB}}} \quad (26)$$

where $q(t_w)$ is the heat flux as a function of the surface temperature [W·m^{-2}]; t_w is the sheet surface temperature (subscript w from "wall") [°C]; t_{DTB} and t_{EFB} are the values of the surface temperature at the reference points DTB (Departure of Transient Boiling) and EFB

[4] Used in blocks 7-9 of the diagram in Figure 2.

Preprints (www.preprints.org) | NOT PEER-REVIEWED | Posted: 17 June 2022 doi:10.20944/preprints202206.0249.v1

(End of Film Boiling) respectively [°C]; q_{DTB} and q_{EFB} are the values of the heat flux at the DTB and EFB reference points [W·m^{-2}].

To implement the described approach, the coordinates (i.e., temperature and heat flux density) of all reference points of boiling curves for each water cooling zone are calculated in the model.

The *End of Film Boiling temperature* t_{EFB} [°C] is calculated by the formula proposed by the authors:

$$t_{\mathrm{EFB}} = t_{int} + \left(t_{int} - t_f\right)\left(\frac{\rho_f c_f}{\lambda_w \rho_w c_w}\right)^{1/2} k_\tau^{1/2}\mathrm{Re}^{1/3} \quad (27)$$

where t_{int} is the temperature at the liquid-solid interface at EFB point [°C]:

$$t_{int} = t_s + \xi\left(t_{f,lim} - t_s\right) \quad (28)$$

t_s is the liquid saturation temperature [°C]; t_f is the current liquid temperature away from the cooled surface [°C]; $t_{f,lim}$ is the practical limit of the maximum achievable liquid phase temperature when impulse heating [°C], for water at atmospheric pressure we accepted $t_{f,lim}$ = 300 °C according to [49]; ξ is the subcooling effect coefficient, for water at atmospheric pressure:

$$\xi = 0.4 + 0.004 \cdot \Delta t_{sub} \quad (29)$$

Δt_{sub} is the value of liquid subcooling [°C]:

$$\Delta t_{sub} = t_s - t_f \quad (30)$$

ρ_f and c_f are the density [kg·m^{-3}] and true isobaric specific mass heat capacity [J·kg^{-1}K^{-1}] of liquid at the temperature of t_f respectively; λ_w, ρ_w and c_w are the thermal conductivity [W·m^{-1}·K^{-1}], density [kg·m^{-3}] and true isobaric specific mass heat capacity [J·kg^{-1}K^{-1}] of the subsurface layer of cooled sheet at the temperature of t_w respectively (see below); Re is Reynolds number in the form:

$$\mathrm{Re} = \frac{2u_f}{\nu_f}\sqrt{\frac{\sigma_{fs}}{g\left(\rho_{fs} - \rho_{vs}\right)}} \quad (31)$$

u_f is the liquid speed [m·s^{-1}]; ν_f is the kinematic viscosity of the liquid [m^2·s^{-1}]; σ_{fs} is the surface tension coefficient of liquid at the saturation temperature [N·m^{-1}]; g is gravitational acceleration [m·s^{-2}]; ρ_{fs} and ρ_{vs} – the density [kg·m^{-3}] of liquid and vapor at the saturation temperature respectively; k_τ is the model parameter [W·m^{-1}·K^{-1}], that specifies the value of turbulent thermal conduction of the liquid depending on Reynolds number, for the conditions in question k_τ = 0.016 W·m^{-1}·K^{-1}.

Formula (27) follows from the well-known solution for the temperature, which is set at the boundary of two semi-infinite rods at the moment of their contact [50] (p. 401), with the following assumptions: 1) the molecular thermal conductivity of a liquid is negligibly small compared to its turbulent thermal conductivity; 2) the turbulent thermal conductivity is a power function of the Reynolds number:

$$\lambda_\tau = k_\tau \mathrm{Re}^{2/3} \quad (32)$$

where λ_τ is the turbulent thermal conductivity [W·m^{-1}·K^{-1}].

Expression (29) is a linear interpolation of the dependence subcooling effect coefficient ξ on water subcooling in the range of its possible variation from 0.4 to 0.8 (this range for ξ is justified by the authors by analyzing the frequency of potential contacts of liquid with solid surface during oscillations of the liquid-gas interface phases near the EFB temperature).

In the presence of oxide scale on the steel surface, the thermophysical properties of the cooled subsurface layer used in the formula (27) are calculated as follows (values of all properties are understood at temperature t_w):

– density [kg·m^{-3}]:

Preprints (www.preprints.org) | NOT PEER-REVIEWED | Posted: 17 June 2022 doi:10.20944/preprints202206.0249.v1

$$\rho_w = \rho_{met}(1 - \psi_{sc}) + \rho'_{sc}\psi_{sc} \quad (33)$$

where ρ_{met} is the density of steel; ρ'_{sc} is the apparent (i.e. including pores) density of oxide scale; ψ_{sc} is the volume fraction of oxide scale (including pores) in subsurface layer;

– thermal conductivity [W·m^{-1}·K^{-1}]:

$$\lambda_w = \left[\frac{1 - \psi_{sc}}{\lambda_{met}} + \frac{\psi_{sc}}{\lambda_{sc}}\right]^{-1} \quad (34)$$

λ_{met} is the thermal conductivity of steel; λ_{sc} is the thermal conductivity of oxide scale;

– true isobaric specific mass heat capacity [J·kg^{-1}K^{-1}]:

$$c_w = c_{met}(1 - \varepsilon_{sc}) + c_{sc}\varepsilon_{sc} \quad (35)$$

c_{met} is the true isobaric specific mass heat capacity of steel; ε_{sc} is the mass fraction of oxide scale in subsurface layer.

Values of all thermophysical properties in formulas are understood at temperature t_w; thus, for steel, the well-known formulas approximating the dependence of such properties on temperature are used (for example, [51]), and for scale, the authors' formulas described in works [52-55] are taken.

The *End of Transient Boiling temperature* t_{ETB} [°C] is calculated by the formula:

$$t_{ETB} = t_s + \Delta t^0_{ETB} k_w \quad (36)$$

where t_s is the water saturation temperature [°C]; Δt^0_{ETB} is the overheating of the surface in ETB point for a subcooled water at free convection, i.e. without taking into account the water speed [°C]:

$$\Delta t^0_{ETB} = 50 s_{sub} - \Delta t_{sub} \quad (37)$$

s_{sub} is the coefficient of influence of water subcooling on the first critical heat flux at free convection [56] (p. 205):

$$s_{sub} = 1 + 0.065 \frac{\bar{c}_f \Delta t_{sub}}{r_v} \left(\frac{\rho_{fs}}{\rho_{vs}}\right)^{0.8} \quad (38)$$

$\bar{c}_f$ is the average isobaric specific mass heat capacity of water in the range from t_f to t_s [J·kg^{-1}K^{-1}]; r_v is the latent heat of vaporization of water [J·kg^{-1}]; ρ_{fs} and ρ_{vs} are the density of water and vapor at the saturation temperature respectively [kg·m^{-3}]; k_w is the coefficient of influence of water flow velocity on ETB temperature:

$$k_w = \left(1 + 1.5 u_f^{2/3}\right)^{1/4} \quad (39)$$

u_f is the water speed relative to the sheet surface [m·s^{-1}].

Formula (37) is based on the assumption that the heat transfer coefficient at the first critical point (i.e. in ETB point) when the liquid is supercooled remains the same as for a saturated liquid. The validity of this assumption is confirmed, for example, by the experimental data cited in [57, 58]. Formula (39) is based on the assumption that the volume vapor content of the near-wall layer in the first critical state (in ETB point) does not depend on the fluid flow speed.

The *heat flux* at the referents points is calculated on the basis of known methods:

– at the *End of Film Boiling* (i.e., at the EFB-point) – according to Wang-Shi [59],

– at the *End of Transition Boiling* (at the ETB-point) - on the Kutateladze method for the Critical Heat Flux [60] (p. 311), [61] (p. 289),

– at the *End of Nucleate Boiling* (at the ENB-point) – according to Isachenko-Kushnyrev [62] (p. 178).

2.1.3. Microstructure[5]

[5] Used in block 10 of the diagram in Figure 2.

Preprints (www.preprints.org) | NOT PEER-REVIEWED | Posted: 17 June 2022 doi:10.20944/preprints202206.0249.v1

The evolution of the microstructure in the sheet during cooling is predicted from isothermal Time-Temperature-Transformation (TTT-) diagrams [63, 64], [65] (p. 356), using a step-by-step calculation scheme based on the additivity rule [66-68].

In order to use the TTT-diagrams originally presented in graphical form (see example in Figure 9a) the authors modified the method of *approximation by reference points* proposed in [69], [70] (p. 43). The essence of such modification is that in addition to the two reference points - at the beginning and at the "nose" of the C-shaped curve – another reference point below the “nose” is introduced (Figure 9b). This make it possible to significantly improves the approximation accuracy, especially in the lower part of the C-curve, i.e., at temperatures predominantly related to the bainite transformation.

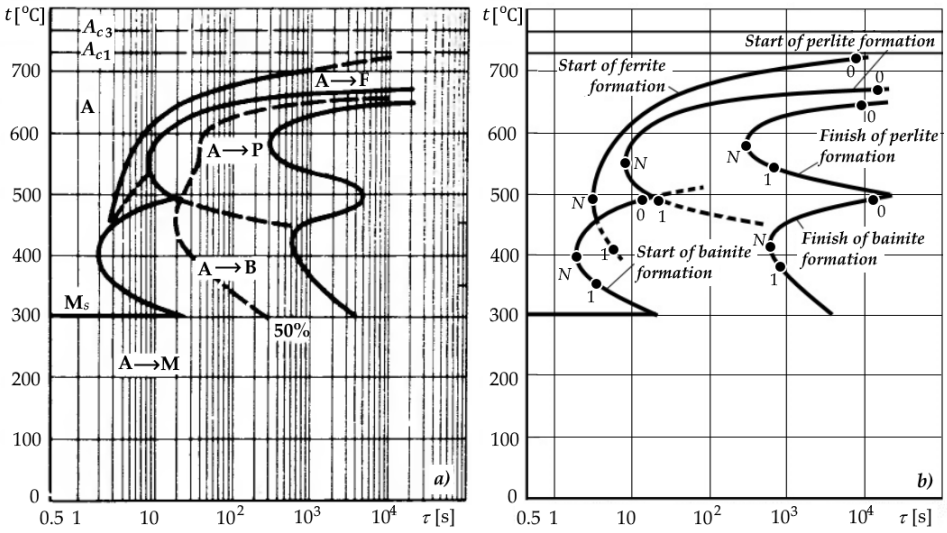

Figure 9. Experimental TTT-diagram for 45G2 steel (*a*) (adapted from [64] (p. 106)) and its C-curves calculated by the 3-point approximation scheme (*b*). Diagram *b*) shows the reference points taken in the approximation for each C-curve: 0 - upper, N - "nose", 1 – lower.

The method of 3-point approximation proposed by the authors allows each of the five basic C-shaped curves of the austenite isothermal transformation (start of ferrite formation, start and finish of pearlite formation, start and finish of bainite transformation) to be described by a single-parameter function of the following form:

$$y = w^c e^{c(1-w)} \tag{40}$$

where y is the function of the logarithm of isothermal holding time τ (as an independent coordinate of the TTT-diagram), w is the function of temperature t (as a dependent coordinate), c is the parameter to be calculated by formula:

$$c = \frac{\ln y_1}{1 - w_1 + \ln w_1} \tag{41}$$

The functions of coordinates in formulas (40)-(41) are as follows:

$$y = \frac{S - S_0}{S_N - S_0} \tag{42}$$

$$w = \frac{U - U_0}{U_N - U_0} \tag{43}$$

$$y_1 = \frac{S_1 - S_0}{S_N - S_0} \tag{44}$$

$$w_1 = \frac{U_1 - U_0}{U_N - U_0} \tag{45}$$

where S means the logarithm of time:

Preprints (www.preprints.org) | NOT PEER-REVIEWED | Posted: 17 June 2022 doi:10.20944/preprints202206.0249.v1

$$S_0 = \ln \tau_0,\ S_N = \ln \tau_N,\ S_1 = \ln \tau_1,\ S = \ln \tau \quad (46)$$

and U means the inverse temperature:

$$U_0 = 1000/t_0,\ U_N = 1000/t_N,\ U_1 = 1000/t_1,\ U = 1000/t \quad (47)$$

subscript "0" refers to the upper reference point (at the beginning of C-curve), "N" - to the reference point at the C-curve "nose", 1 - to the lower reference point (see Figure 9b).

Within the above scheme of using TTT-diagrams to predict the steel microstructure during cooling, *the kinetics of isothermal austenite decomposition* into ferrite and pearlite is calculated by the Kolmogorov-Johnson-Mehl-Avrami (KJMA) equation [71] (p. 128, 496), the bainite transformation - by the Austin-Rickett equation [72, 73], and the martensite transformation - by the Koistinen_Marburger equation [74].

2.1.4. Temperature distribution across the thickness of the sheet[6]

A procedure for numerically solving the one-dimensional unsteady thermal conductivity equation for a flat metal plate with oxide scale on both wide surfaces with boundary conditions of the third kind has been implemented.

The design scheme is shown in Figure 10. Designations in this figure are as following: H is the sheet thickness including oxide scale; h_{sb} and h_{st} are the thickness of oxide scale layer on the bottom and top surface respectively; h_m is the thickness of metal body without oxide scale; $n_{sb} \geq 3$ is the quantity of nodes of the computation grid inside the bottom oxide scale layer (the quantity of nodes inside the top oxide scale layer should also be not less than 3); n_m is the quantity of nodes of the computation grid inside the metal body; n is the total quantity of nodes across the thickness of the sheet with oxide scale (the value of n is determined automatically, based on the thickness of the elementary layer Δx specified in the initial data); i is the number of the current node; δ_b and δ_t are the thickness of internal elementary layer of the bottom and top oxide scale respectively; Δx is the thickness of internal elementary layer of the metal body.

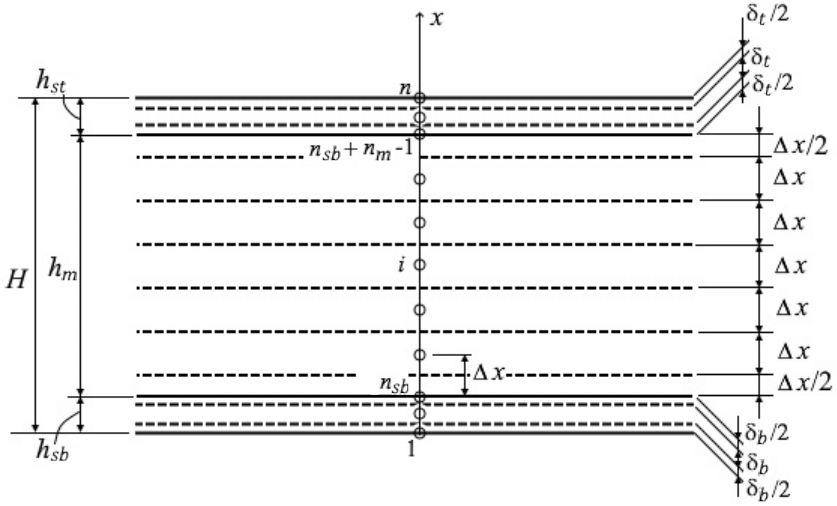

Figure 10. The design scheme for numerical calculation of the sheet temperature (x is the axis along the thickness of the sheet). Designations are in the text.

The finite-difference equations to be solved at any time step except the initial one (i.e. at time $\tau > 0$) are as follows:

– inside the metal body ($n_{sb} + 1 \leq i \leq n_{sb} + n_m - 2$):

$$c_i^k \rho_i^k \frac{t_i^{k+1} - t_i^k}{\Delta\tau} = \lambda_i^k \cdot \frac{t_{i+1}^{k+1} - 2t_i^{k+1} + t_{i-1}^{k+1}}{(\Delta x)^2} + q_{Vi} \quad (48)$$

[6] Used in block 11 of the diagram in Figure 2.

Preprints (www.preprints.org) | NOT PEER-REVIEWED | Posted: 17 June 2022 doi:10.20944/preprints202206.0249.v1

where t_i^k is the temperature in the i-th node at the k-th point in time [°C]; $\Delta\tau$ is the time step between the k-th and k+1-th points in time [s]; c_i^k, ρ_i^k and λ_i^k are the values of the properties of steel in the i-th node at the k-th point in time: isobaric specific mass heat capacity [J·kg^{-1}K^{-1}], density [kg·m^{-3}] and thermal conductivity [W·m^{-1}·K^{-1}] respectively; q_{Vi} is the volumetric latent heat capacity of phase transformations in steel [W·m^{-3}] (values for austenite transformation are taken from [75]);

– inside the bottom scale layer ($2 \le i \le n_{sb} - 1$):

$$c_{sci}^k \rho_{sci}^k \frac{t_i^{k+1} - t_i^k}{\Delta\tau} = \lambda_{sci}^k \cdot \frac{t_{i+1}^{k+1} - 2t_i^{k+1} + t_{i-1}^{k+1}}{\delta_b^2}, \quad (49)$$

c_{sci}^k, ρ_{sci}^k and λ_{sci}^k are the values of the properties of oxide scale in the i-th node at the k-th point in time: isobaric specific mass heat capacity [J·kg^{-1}K^{-1}], density [kg·m^{-3}] and thermal conductivity [W·m^{-1}·K^{-1}] respectively;

– inside the top scale layer ($n_{sb} + n_m \le i \le n - 1$):

$$c_{sci}^k \rho_{sci}^k \frac{t_i^{k+1} - t_i^k}{\Delta\tau} = \lambda_{sci}^k \cdot \frac{t_{i+1}^{k+1} - 2t_i^{k+1} + t_{i-1}^{k+1}}{\delta_t^2} \quad (50)$$

– conjugation conditions between the bottom scale layer and the metal ($i = n_{sb}$):

$$\frac{\lambda_i^k}{\Delta x}(t_{i+1}^{k+1} - t_i^{k+1}) = \frac{\lambda_{sci}^k}{\delta_b}(t_i^{k+1} - t_{i-1}^{k+1}) \quad (51)$$

– conjugation conditions between the top scale layer and the metal ($i = n - n_m + 1$):

$$\frac{\lambda_i^k}{\Delta x}(t_i^{k+1} - t_{i-1}^{k+1}) = \frac{\lambda_{sci}^k}{\delta_t}(t_{i+1}^{k+1} - t_i^{k+1}) \quad (52)$$

– boundary conditions at the bottom scale surface ($i = 1$):

$$\alpha_b^k(t_i^{k+1} - t_{ab}^{k+1}) - \frac{\lambda_{sci}^k}{\delta_b}(t_{i+1}^{k+1} - t_i^{k+1}) = -c_{sci}^k \rho_{sci}^k \frac{\delta_b}{2}\left(\frac{t_i^{k+1} - t_i^k}{\Delta\tau}\right) \quad (53)$$

α_b^k is the heat transfer coefficient at the bottom surface of the sheet at the k-th point in time [W·m^{-2}·K^{-1}]; t_{ab}^{k+1} is the ambient temperature at the bottom surface at the k+1-th point in time [°C];

– boundary conditions at the top scale surface ($i = n$):

$$\alpha_t^k(t_n^{k+1} - t_{at}^{k+1}) + \frac{\lambda_{sci}^k}{\delta_t}(t_i^{k+1} - t_{i-1}^{k+1}) = -c_{sci}^k \rho_{sci}^k \frac{\delta_t}{2}\left(\frac{t_i^{k+1} - t_i^k}{\Delta\tau}\right). \quad (54)$$

α_t^k is the heat transfer coefficient at the top surface at the k-th point in time [W·m^{-2}·K^{-1}]; t_{at}^{k+1} is the ambient temperature at the top surface at the k+1-th point in time [°C].

The system of n equations (48)-(54) is solved using an implicit finite-difference scheme by the Thomas (tridiagonal matrix) algorithm [76] (p. 83). The step of the calculation grid over the thickness of the sheet Δx is about 0.1 mm, the basic time step $\Delta\tau$ is about 0.1 s (additionally divided by the borders between the design cooling zones on the top and bottom surfaces of the sheet).

2.2. Experimental studies

2.2.1. Experiment procedure

In order to check the adequacy and to adapt the model, the authors used the data of previously conducted temperature measurements across the thickness of the steel plate during processing in a roller quenching machine (RQM) of NKMZ design [77].

The technique of experimental studies is described in detail in [78, 79]. Its essence was the application of a measuring complex in the form of a test plate with embedded thermocouples, connected to the data collection and recording system (Figure 11).

The experiments involved two test plates of a structural carbon steel 45 (standard chemical composition in weight is C=0.42…0.5%, Si=0.17…0.37%, Mn=0.5…0.8%) with dimensions of 30x2000x4000 mm. Four thermocouples were embedded in each of them (see scheme in Figure 12): in the first plate there have been three thermocouples in the middle

Preprints (www.preprints.org) | NOT PEER-REVIEWED | Posted: 17 June 2022 doi:10.20944/preprints202206.0249.v1

of the width (one at the top, bottom and center of the thickness), one at the top at a distance of 200 mm from the lateral edge; in the second plate - two thermocouples in the middle of the width (one at the top and bottom) and two at a distance of 200 mm from the lateral edge (one at the top and bottom). The depth of the surface thermocouples was 3 and 2.5 mm from the top and bottom surface, respectively. A total of two series of five tests each were performed. The first plate was used in tests Nos. 1-5, and the second plate in tests Nos. 6-10.

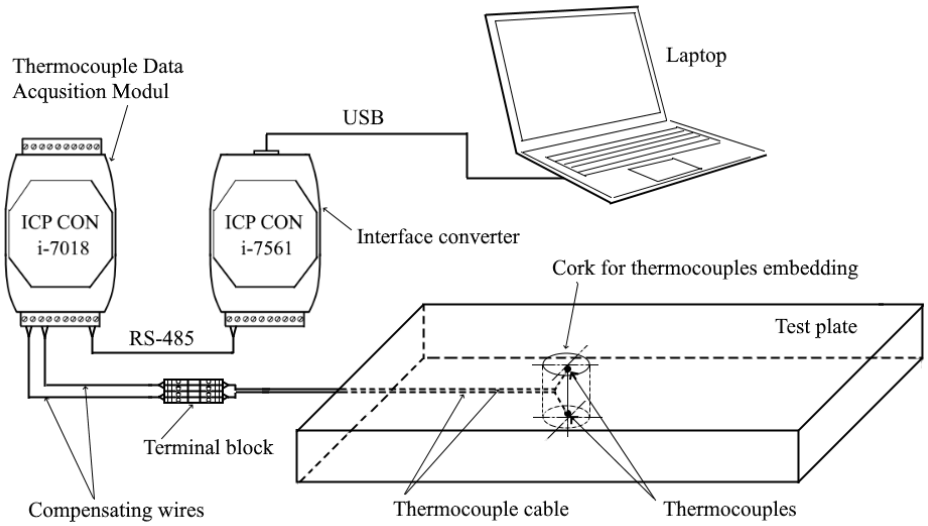

Figure 11. Schematic of the measuring complex.

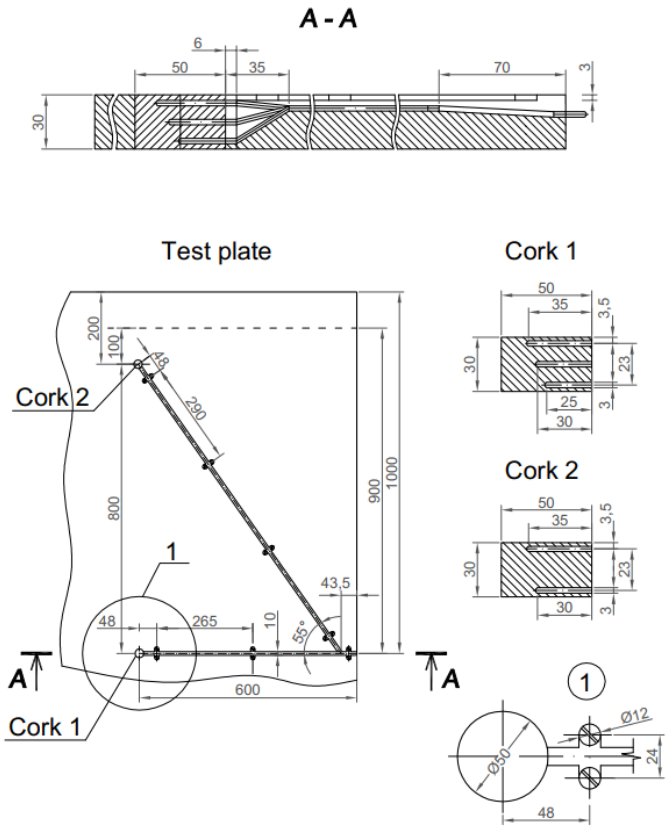

Figure 12. Thermocouples embedding scheme (dimensions are in mm). Of the five channels prepared, four were used in each test plate (details in the text).

Preprints (www.preprints.org) | NOT PEER-REVIEWED | Posted: 17 June 2022 doi:10.20944/preprints202206.0249.v1

The scheme of each test involved charging a cold plate with thermocouples into a heating furnace from the RQM side (i.e., through the furnace outlet window), heating it to a preset temperature, discharging from the furnace at a constant speed and cooling in the roller quenching machine. The heating temperature and RQM operating regime in each test are given in Table 1.

The signals from thermocouples were recorded continuously during the whole process of heating the test plate in the furnace, its transportation and subsequent cooling in the RQM. As an example, Figure 13 shows plots of temperature measured at different control points of the plate during a single test (No. 2). The temperature measurements in the furnace (i.e., for the time from t_0 to t_1) were used to calculate the thickness of the oxide scale layer on the plate surface. The measurement data after the plate was discharged from the furnace (after t_1) was compared with the results of the cooling model calculation.

Table 1. Setpoint heating temperature and RQM operating regime in tests.

Test No.	Heating temperature [°C]	Plate speed [ms^{-1}]	Water temperature [°C]	Water flow rates by RQM zones*: top (above the line) and bottom (below the line) [m^{3}h^{-1}]						
				H1	H2-3	L1-2	L3	L4	L5	L6
1	850	0.12	23	530	290	110	110	110	0	0
				510	510	190	190	190	0	0
2	950	0.11	23	310	290	110	110	110	0	0
				510	510	190	190	190	0	0
3	950	0.11	23	0	290	110	110	110	75	0
				0	490	190	190	190	115	0
4	950	0.11	23	310	100	110	110	110	70	0
				510	180	190	190	190	115	0
5	950	0.11	23	310	0	110	110	110	0	0
				510	0	190	190	190	0	0
6	950	0.11	34	0	120	130	130	90	130	130
				0	210	210	210	160	210	210
7	950	0.11	34	310	0	130	110	110	75	0
				310	200	190	153	170	115	0
8	950	0.09	34	310	0	130	0	110	75	0
				310	200	190	0	170	115	0
9	950	0.09	33	310	0	130	0	110	75	0
				210	200	190	0	170	115	0
10	980	0.11	32	310	100	0	0	90	110	75
				410	175	0	0	155	170	115

*The designations of RQM zones mean: type (H – High-intensive, L - Low-intensive) and ordinal number (H2-3 and L1-2 are paired zones with twin banks)

2.2.2. Estimation of oxide scale thickness on the surface of the test plates

We accepted the diffusion mechanism of oxide scale growth, according to which the rate of its mass increase is inversely proportional to the mass of already formed scale [80] (p. 49):

$$\frac{dY}{d\tau} = \frac{K^2}{2Y} \tag{55}$$

where Y is scale mass per unit surface [kg·m^{-2}]; τ is time [s]; K is an oxidation rate constant [kg·m^{-2}s$^{-0,5}$].

Integration of (55) gives a parabolic equation of scale growth [81]:

Preprints (www.preprints.org) | NOT PEER-REVIEWED | Posted: 17 June 2022 doi:10.20944/preprints202206.0249.v1

$$Y^2 = Y_0^2 + K^2\tau \quad (56)$$

where Y_0 is scale mass per unit surface [kg·m^{-2}] at τ = 0 s.

Differential equation (55) is non-linear, because the oxidation rate constant changes in time with temperature change [82] (p. 59):

$$K = A \cdot \exp\left(-\frac{B}{T}\right) \quad (57)$$

where T is an absolute temperature in degrees Kelvin, A and B are material parameters. For steel 45 the values of these parameters were taken according to [83] (p. 146) as A = 11.41 kg·m^{-2}s$^{-0,5}$, B = 8274 K.

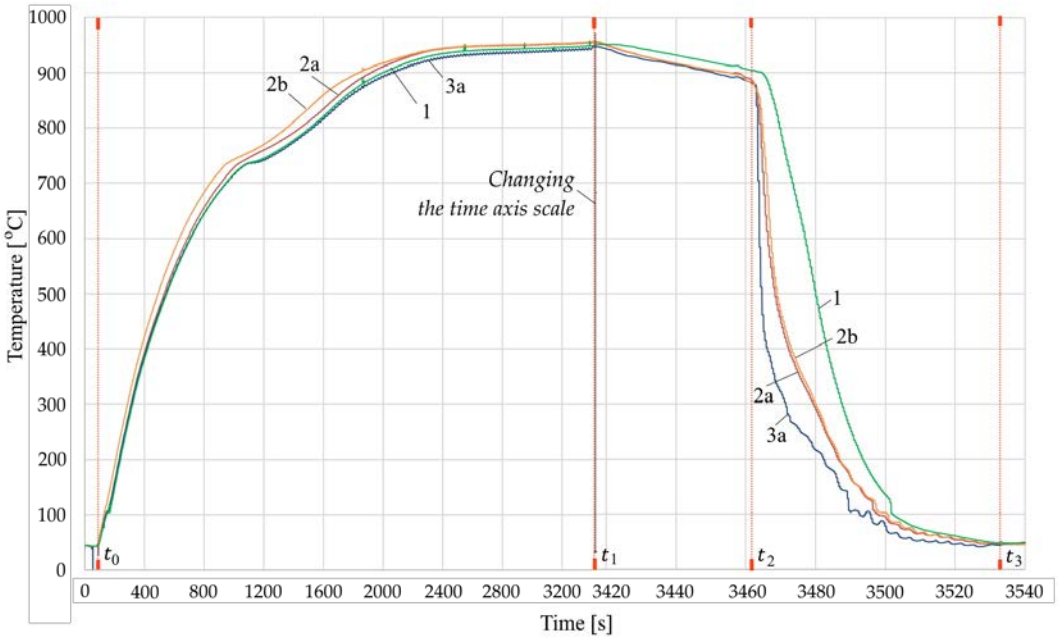

Figure 13. Plots of temperature changes, measured by thermocouples in test No. 2 during heating and cooling. Designations of the curves: 1 - at the center of the thickness in the middle of the plate width, 2a - at the top in the middle of the width, 2b -at the top at the edge, 3a - at the bottom in the middle of the width. Designations of the key moments of time: t_0- entry into the furnace; t_1 - exit from the furnace; t_2 - entry into the first zone of RQM; t_3 - exit from RQM

To numerically solve differential equation (55) we used Euler's method by explicit finite-difference scheme:

$$Y_{i+1} = Y_i + \frac{A^2}{2Y_i} \cdot \exp\left(-\frac{2B}{T_i}\right)\Delta\tau \quad (58)$$

where Y_i and Y_{i+1} are specific mass of oxide scale at the beginning and at the end of the i-th time interval [kg·m^{-2}]; T_i is the surface temperature measured at the beginning of the i-th time interval, K; $\Delta\tau$ is a measurement cycle, which was equal to 0.07 s.

Transition from specific mass to scale thickness was carried out as follows:

$$h_i = \frac{Y_i}{(1-\eta_{sc})\,\rho_{sc}} \quad (59)$$

where h_i is the oxide scale thickness corresponding to its specific mass Y_i [m]; η_{sc} is the porosity of oxide scale in fractions of one; ρ_{sc} is its true density [kg·m^{-3}]. For furnace scale, formed when heated to 850-980 ºC we assumed η_{sc} = 0.15 [84] and ρ_{sc} = 5500 kg·m^{-3} [52].

Using the described procedure, we calculated the thickness of oxide scale at the exit of the furnace before each test. In this case, given that visually on the upper surface of the plates after processing in RQM rough scale was not observed, the initial thickness of the

 doi:10.20944/preprints202206.0249.v1

oxide layer at charging into the furnace was taken zero (more precisely, 1 micron in order to avoid dividing by zero in the formula (58) for the first cycle of measurements). The calculated values of the scale thickness at the exit of the furnace are provided in Table 2.

Table 2. Measured temperature and calculated scale thickness at the exit of the furnace on the top (above the line) and the bottom (below the line) surface of the plate*.

Test No.	Total heating time [min-sec]	Plate temperature [°C]	Oxide scale thickness [μm]
1	47′10″	853	47
		845	42
2	55′27″	956	113
		948	103
3	46′16″	957	105
		950	97
4	43′57″	956	105
		949	95
5	43′30″	956	103
		950	94
6	56′28″	962	104
		958	98
7	52′23″	958	123
		954	116
8	51′48″	957	123
		951	117
9	45′29″	958	110
		950	104
10	60′43″	982	147
		976	138

*In tests, in which there have been two thermocouples on one surface, the final values of temperature and scale thickness for the entire surface are taken by averaging the data for both points.

3. Results

According to the authors' cooling model, calculations were performed for the conditions of each of the ten tests. Values of the basic input data (in addition to the data presented in Table 1, Table 2 and Figure 12) were taken as follows:

– design and layout characteristics of RQM - according to the technical documentation of the equipment manufacturer (basic characteristics are given in works [27, 77, 85]);

– thermophysical properties of test plate as a function of temperature – according to the formulas [51] for medium-carbon steel**Appendix A**;

– thermophysical properties of oxide scale as a function of temperature - according to the authors' formulas [52-55];

– oxide scale thickness was assumed constant throughout the cooling period of each test and equal to the values given in Table 2.

The results of calculations in comparison with the corresponding experimental data are presented in the form of graphs of temperature changes over time. For example, Figure 14, Figure 15 and Figure 16 compare experimental and calculated graphs for tests

Preprints (www.preprints.org) | NOT PEER-REVIEWED | Posted: 17 June 2022 doi:10.20944/preprints202206.0249.v1

No. 3, No. 5 and No. 10 respectively. Appendix A shows similar graphs for the remaining seven tests.

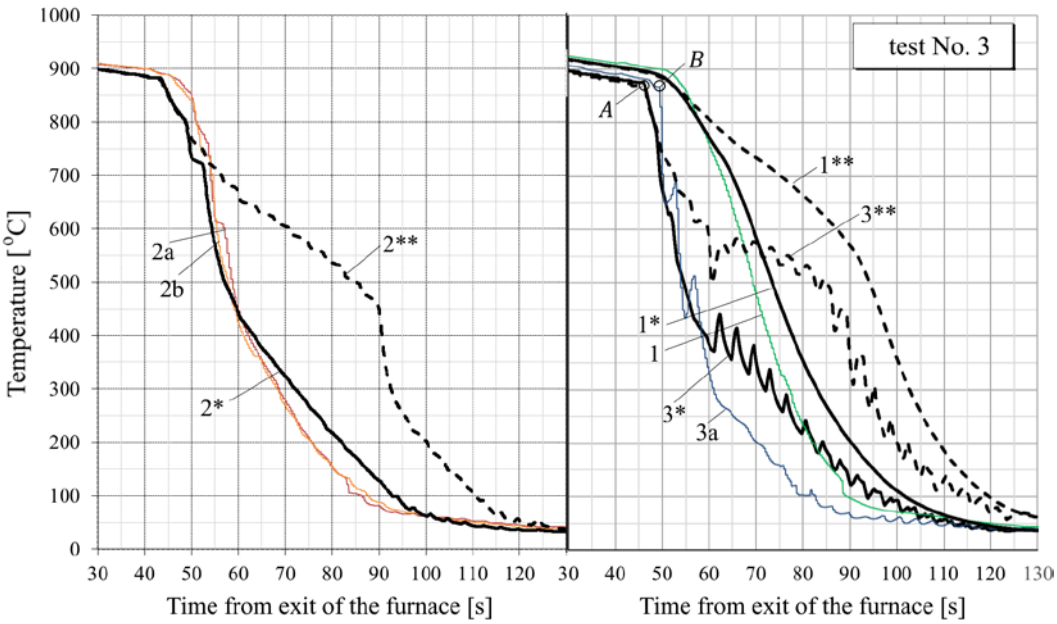

Figure 14. Graphs of cooling in the test No. 3. Numbers without an asterisk denote experimental curves according to the thermocouple data: 1 –at the center of the thickness in the middle of the plate width, 2a - at the top in the middle of the width, 2b - at the top at the edge, 3a - at the bottom in the middle of the width. Numbers with one asterisk indicate calculated curves for the corresponding control points across the thickness of the plate: 1* - at the center of the sheet thickness, 2* - at the depth of 3 mm from the top surface, 3* - at the depth of 2.5 mm from the bottom surface. For comparison, the calculated curves obtained without regard to scale are given (marked with the same numbers, but with two asterisks). Point A is the first inflection of the calculated temperature graph, corresponding to the beginning of water cooling from below, point B is the same in the test (its lag for several seconds is probably due to thermal inertia of the thermocouple).

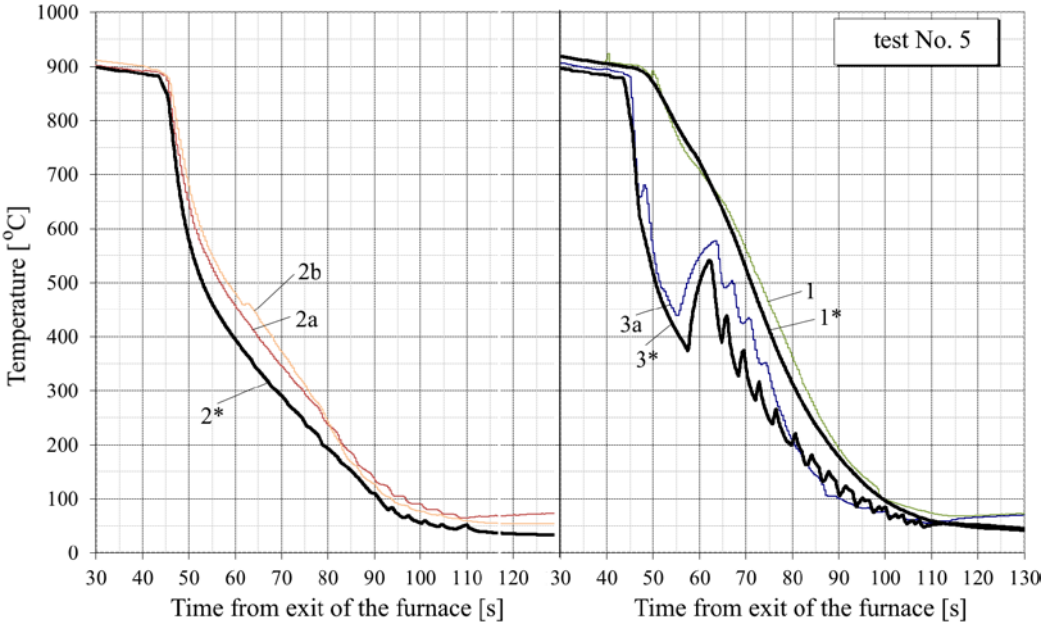

Figure 15. Graphs of cooling in test No. 5. The notations are the same as in Figure 14.

Preprints (www.preprints.org) | NOT PEER-REVIEWED | Posted: 17 June 2022 doi:10.20944/preprints202206.0249.v1

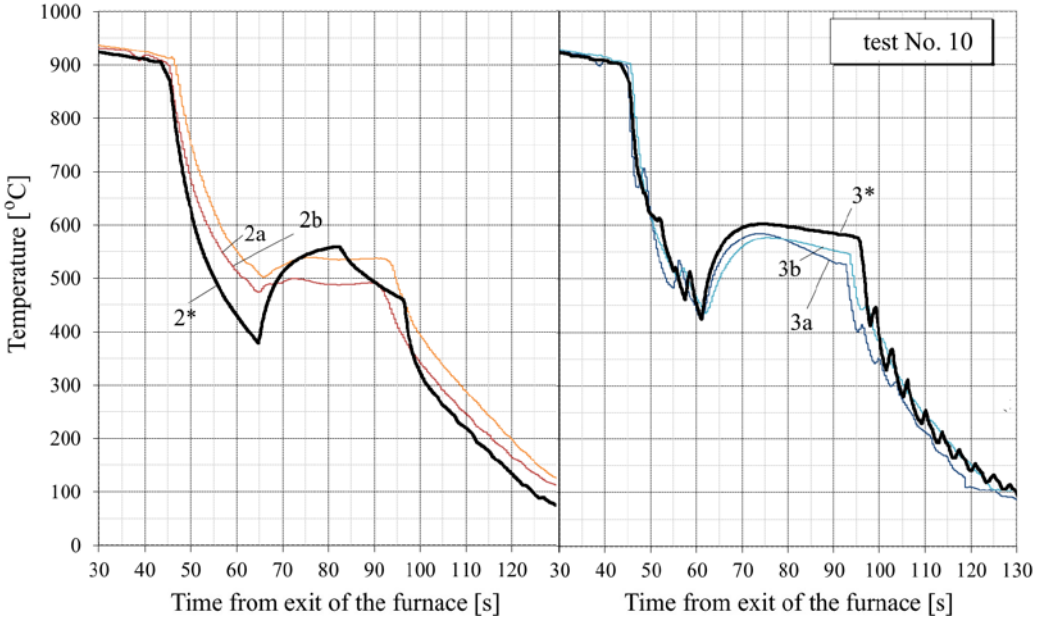

Figure 16. Graphs of cooling in the test No. 10. Numbers without an asterisk denote experimental curves according to the thermocouple data: 2a - at the top in the middle of the width, 2b - at the top at the edge, 3a - at the bottom in the middle of the width, 3b - at the bottom at the edge. Numbers with one asterisk indicate calculated curves for the corresponding control points across the thickness of the plate: 2* - at the depth of 3 mm from the top surface, 3* - at the depth of 2.5 mm from the bottom surface.

Analysis of the data obtained shows the following.

1) For all tests, the calculated temperature at the RQM outlet corresponds to the measured one with deviations do not exceed 10 °C. So, the total heat loss of the sheet is taken into account correctly, which indirectly confirms the adequacy of calculation of the first and second critical surface temperatures corresponding to the change of film, transition and nucleate boiling regimes (i.e. the EFB and ETB temperature in Figure 8).

2) In tests with interrupted cooling (Nos. 5, 8, 9, and 10 - see Figure 15, Figure 16, Figure A6, Figure A7) the calculated temperature graphs repeat the characteristic changes in the course of experimental curves. This suggests that the sizes of characteristic zones of jet cooling, as well as the parameters of water spreading over the top and bottom surfaces of the sheet, are correctly taken into account.

3) The degree of closeness of calculated and experimental curves remains approximately at the same level at significantly different water temperatures (from 23 °C in tests Nos. 1-5 to 32-34 °C in tests Nos. 6-10), which indicates the correctness of taking into account this factor in the model.

4) Scale thickness on the plate surface is the main parameter of the model which defines its agreement with experiment. For comparison, Figure 14 shows also the graphs for test No. 3, calculated without taking scale into account (dotted curves marked by the numbers with two asterisks). It can be seen that in this case there are very rough discrepancies between the calculated and experimental data.

5) In tests Nos. 2, 3, 6 and 7 (Figure 14, Figure A2, Figure A4 and Figure A5) in the area of surface thermocouple readings below 400-450 °C, the calculated temperature is much higher than the experimental one. In our opinion, this is due to the assumption adopted in the simulation of constant thickness of the scale during the entire cooling period. This assumption is generally not true, because during accelerated cooling, oxide scale can crack and be removed (partially or completely) from the sheet surface by water jets. At the same time, the influence of scale depends on the water boiling regime: at high temperatures corresponding to film and transient boiling, oxide scale, as a rule, increases the intensity of heat transfer to the surface, and at stable nucleate boiling, on the contrary,

Preprints (www.preprints.org) | NOT PEER-REVIEWED | Posted: 17 June 2022 doi:10.20944/preprints202206.0249.v1

reduces it [86]. Therefore, if oxide scale is removed from the sheet surface after stable nucleate boiling is achieved, it is accompanied by an increase in the intensity of cooling. In spray cooling, stable nucleate boiling of water usually begins at 200-250 °C at the surface, which at the corresponding heat flux values approximately corresponds to a temperature of 400-450 °C at a depth of 2.5-3 mm (for a plate 30 mm thick). This explains the above-mentioned overestimation of the calculated temperature in the noted experiments with surface thermocouple readings below 400-450 °C. This effect is also confirmed by model calculations. For example, in Figure 14 it is seen that at indications of surface thermocouples above 400-450 °C the slope angle of experimental plots is close to the slope angle of design graphs with scale, and below this boundary - to the slope angle of design graphs without scale.

6) Practically in all cases there is a "lag" for 1-3 seconds of the experimental curves from the calculated ones at the very beginning of intensive cooling (see, for example, points A and B in Figure 14). This, most likely, can be explained by thermal inertia of thermocouples [87], which is manifested to the greatest extent at a sharp change of metal temperature.

7) To quantify the "proximity" of the experimental and calculated graphs, the value of the average cooling rate in a certain temperature interval was used. Table 3 summarizes the average cooling rate in the three typical temperature ranges: 800-400 °C, 400-200 °C and 200-100 °C. The value in each cell of this table is obtained by averaging over all experiments. It can be seen that calculated cooling rates are in general somewhat lower than experimentally determined (on average by 12-20% in different temperature intervals). Higher cooling rates in experiments (than in the simulation) can be explained by the factors mentioned above: thermal inertia of thermocouples (see item 6) and scale removal from the plate surface during cooling in RQM (see item 5). In this case, if the thermal inertia of thermocouples affects only the "apparent" cooling rate, the reduction of the scale layer affects the actual intensity of heat transfer.

Table 3. Average cooling rate in characteristic temperature intervals

Nature of the data	Reference coordinate by sheet thickness*	Average cooling rate [°C/s] in temperature range		
		800-400 °C	400-200 °C	200-100 °C
Experiment (thermocouples)	top	27.5	14.4	8.0
	center	23.7	20.3	11.4
	bottom	42.2	14.3	7.9
Calculation (model)	top	29.4	11.0	8.4
	center	21.2	16.3	9.0
	bottom	32.2	11.9	6.5
Deviation (calculation minus experiment)	top	1.8	-3.5	0.4
	center	-2.5	-4.0	-2.4
	bottom	-10.0	-2.4	-1.5
	averaged over three coordinates**	-3.6 (-12%)	-3.3 (-20%)	-1.1 (-13%)

*Top - 3 mm from the top surface, bottom - 2.5 mm from the bottom surface
**Percentages are relative to experimental values

4. Discussion

The obtained results confirm that the main factor that introduces uncertainty into the process of accelerated cooling of metal in production conditions is oxide scale on its surface. Moreover, we are not talking about the fact that scale, especially peeled scale, distorts the readings of the workshop pyrometers. Much more important is the fact that oxide

scale changes the *real intensity of cooling* because it shifts the boiling curve. When cooling a surface with oxide scale, the boiling curve, in general, is a composition of two curves (Figure 17) [86]: at the initial stage, it follows the boiling curve for the surface covered with a continuous layer of scale, and then, due to scale cracking, it shifts in the direction of the boiling curve for a clean surface. Therefore, in the presence of scale, in general, two more reference points are added to the boiling curve:

SHX - Start sHift due to oXide layer and
EHX - End sHift due to oXide layer.

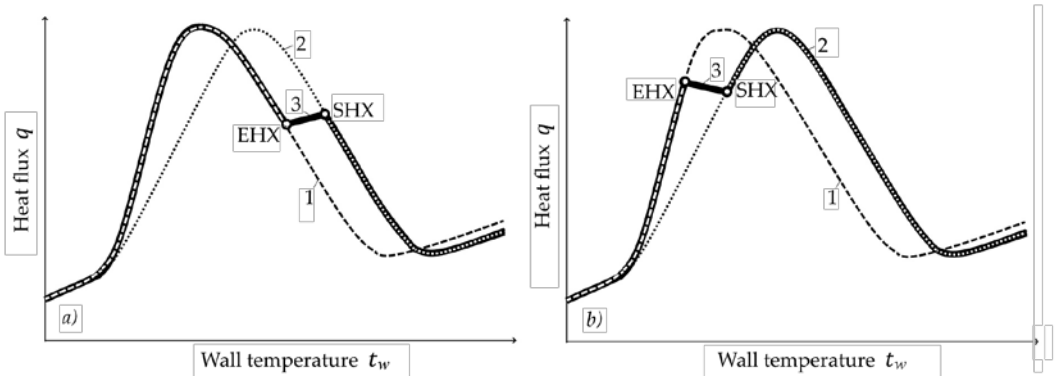

Figure 17. Schematic of the boiling curve formation during water jet cooling on the surface covered by an oxide scale. Boiling curve symbols: 1 (dashed) – on the clear metal surface without oxide scale, 2 (dotted) – on the surface with a hard scale, 3 (solid) - in case of scale cracking. SHX and EHX – the reference points associated with oxide scale (transcript - in the text). Figure (a) shows an example when scale cracking occurs at the transient boiling regime (in this case oxide scale increases heat flux); figure (b) shows an example when scale cracking occurs at the nucleate boiling regime (in this case oxide scale decreases heat flux).

The moment at which this "jump" from one boiling curve to the other occurs (see Figure 17) will determine both the course of the cooling process and the final temperature of the metal. Unfortunately, the cracking and removal of oxide scale from the sheet surface is very difficult to predict because it is a random event, which creates inevitable uncertainty when modeling cooling over a wide temperature range. Moreover, in practice, the initial thickness of the surface scale layer is also usually unknown.

This predetermines two main directions of further research: 1) predicting the thickness of scale during TMCP processing, taking into account its initial thickness, the strength of adhesion with the base metal and the dynamics of failure in the cooling unit, and 2) using the thickness of the oxide scale layer as the main parameter for the on-line adaptation of the temperature model in the ACS of accelerated cooling and quenching units.

Acknowledgments: The authors are grateful to D.O. Kozlenko for developing the software user service of the cooling model and to A.L. Ostapenko for helpful advice in discussing the results of this work.

References

1. Uranga, P.; Rodríguez-Ibabe, J.M. Thermomechanical Processing of Steels. *Metals.* **2020**, 10(5), 641-644. [https://doi.org/10.3390/met10050641]
2. Schwinn, V.; Bauer, J.; Flüss, P.; Kirsch, H-J.; Amoris, E. Recent Developments and Applications of TMCP Steel Plates. *Revue de Métallurgie.* **2011**, 108, 283–294. [https://doi.org/10.1051/metal/2011054]
3. Militzer, M. Thermomechanical Processed Steels. In *Comprehensive Materials Processing*, 1st ed. Hashmi, S. ed. Elsevier: Amsterdam, Netherlands, **2014**, 1, 191-216. [https://doi.org/10.1016/B978-0-08-096532-1.00115-1]
4. Endo, Sh.; Nakata, N. Development of Thermo-Mechanical Control Process (TMCP) and High Performance Steel in JFE Steel. *JFE Tech. Rep.* **2015**, 20, 1-6.

5. Igi, S.; Miyake, M. Development of Thermo-Mechanical Control Process (TMCP) and High Performance Steel in JFE Steel. *JFE Tech. Rep*. **2021**, 26, 86-94.
6. Nishioka, K.; Ichikawa, K. Progress in thermomechanical control of steel plates and their commercialization. *Sci. Technol. Adv. Mater*. **2012**, 13, 20pp. [https://doi.org/10.1088/1468-6996/13/2/023001].
7. Wang, Zh.; Wang, Bingxing; Wang, Bin; Tian, Y.; Zhang, T.; Yuan, G.; Liu, Zh.; Wang G. Development and Application of Thermo-mechanical Control Process Involving Ultra-fast Cooling Technology in China. *ISIJ Int.* **2019**, 59(12), 2131–2141. [https://doi.org/10.2355/isijinternational.ISIJINT-2019-041]
8. Wang, D.; Zang, P.; Peng, X.; Yan, L.; Li, G. Comparison of Microstructure and Mechanical Properties of High Strength and Toughness Ship Plate Steel. *Materials.* **2021**, 14, 5886. [https://doi.org/10.3390/ma14195886]
9. Nowotnik, A.; Siwecki, T. The effect of TMCP parameters on the microstructure and mechanical properties of Ti–Nb microalloyed steel. *J. Microsc.* **2010**, 237, 258–262. [https://doi.org/10.1111/j.1365-2818.2009.03238.x]
10. Paiva, F.; Santos, A.; Buono, V. and Gandra, C. Influence of accelerated cooling conditions on microstructure and flatness of API steel heavy plates. In 56° Seminário de Laminação e Conformação de Metais, São Paulo, 2019. Sao Paulo, SP, Brazil, **2019**, 51-61. [https://doi.org/10.5151/2594-5297-32315]
11. Kirillov, P.L.; Ninokata, H. Heat transfer in nuclear thermal hydraulics. In *Thermal-Hydraulics of Water Cooled Nuclear Reactors*, 1st ed. D'Auria, F. ed. **2017**. 357-492. [http://dx.doi.org/10.1016/B978-0-08-100662-7.00007-5]
12. Liang, G; Mudawar, I. Review of spray cooling – Part 2: High temperature boiling regimes and quenching applications. *Int. J. Heat Mass Transf.*, **2017**, 115, Part A, 1206-1222 [http://dx.doi.org/10.1016/j.ijheatmasstransfer.2017.06.022]
13. Kohler, C.; Jeschar, R.; Scholz, R. Slowik, J.; Borchardt, G. Influence of oxide scales on heat transfer in secondary cooling zones in the continuous casting process. Part 1: Heat transfer through hot-oxidized steel surfaces cooled by spray-water. *Steel Research.* **1990**, 61(7), 295–301.
14. Slowik, J.; Borchardt, G.; Kohler, C.; Jeschar, R.; Scholz, R. Influence of oxide scales on heat transfer in secondary cooling zones in the continuous casting process. Part II: Determination of material properties of oxide scales on the steel under spray-water cooling conditions. *Steel Research.* **1990**, 61(7), 302–311. [https://doi.org/10.1002/srin.199000353]
15. Wendelstorf, J.; Spitzer, K.-H.; Wendelstorf, R. Effect of oxide layers on spray water cooling heat transfer at high surface temperatures. *Int. J. Heat Mass Transf.* **2008**, 51, 4892–4901. [https://doi.org/10.1016/j.ijheatmasstransfer.2008.01.033]
16. Horsky, J.; Hrabovsky, J.; Raudensky M. Impact of the oxide scale on spray cooling intensity. HEFAT2014, Orlando, Fl, USA, **2014**, 1480-1485. [http://hdl.handle.net/2263/44729]
17. Chabičovský, M.; Hnizdil, M.; Tseng, A.; Raudenský, M. Effects of oxide layer on Leidenfrost temperature during spray cooling of steel at high temperatures. *Int. J. Heat Mass Transf.* **2015**, 88, 236-246. [https://doi.org/10.1016/j.ijheatmasstransfer.2015.04.067]
18. Chabičovský, M.; Resl, O.; Raudenský, M. Impact of oxide layer on spray cooling intensity and homogeneity during continuous casting of steel. In Proceedings of Metal'2018, Brno, Czech Republic, EU. **2018**, 69-74.
19. Hernandez-Avila, V.H. Heat transfer model of the hot rolling runout table-cooling and coil cooling of steel. A thesis submitted, Degree of Master in Applied Science, The University of British Columbia, Vancouver, Canada, **1994**, 133 p.
20. Singh, A.P.; Prasad, A.; Prakash, K.; Sengupta, D.; Murty, G.M.D.; Jha, S. Influence of thermomechanical processing and accelerated cooling on microstructures and mechanical properties of plain carbon and microalloyed steels. *Mater. Sci. Technol.* **1999**, 15, 121-126. [https://doi.org/10.1179/026708399101505554]
21. Gomez, G.; Schicht, J.; Perez, T.; Goldschmit, M.; Vigliocco, A. Thermo-metallurgical model of the cooling table for a flat product hot rolling mill. In Proceedings of The Materials Science and Technology Conference, Cincinnati, Ohio, USA, **2006**, 1677–1687.
22. Muhin, U.; Belskij, S.; Makarov, E.; Koynov. T. Simulation of accelerated strip cooling on the hot rolling mill run-out roller table. *Frat. ed Integrità Strutt.* **2016**, 37, 305-311. [https://doi.org/10.3221/IGF-ESIS.37.40]
23. Koldin, A.; Dema, R.; Nalimova, M.; Mihailov, E.; Shapovalov, A.; Kharchenko, M. Modeling of the thermal state of the hot rolled strip in the accelerated cooling process Part 1: Heat transfer model. *J. Chem. Technol. Metall*. **2019**, 54(6), 1330-1336. [https://dl.uctm.edu/journal/node/j2019-6/26_19-88_p_1330-1336.pdf]
24. Liu, W.-W.; Li, H-J.; Wang, Zh.-D.; Wang, G.-D. Mathematical model for cooling process and its self-learning applied in hot rolling mill. *J Shanghai Univ* (Engl. Ed.). **2011**, 15(6), 548–552. [https://doi.org/10.1007/s11741-011-0784-2]
25. Malinowski, Z.; Cebo-Rudnicka, A.; Hadała, B.; Szajding, A.; Telejko, T. Implementation of one and three dimensional models for heat transfer coefficient identification over the plate cooled by the circular water jets. *Heat Mass Transfer*, **2018,** 54, 2195-2213. [https://doi.org/10.1007/s00231-017-2195-0]
26. Ivantsov, O.V.; Kaskin, B.K.; Vaskin, A.M.; Viventsov, A.S.; Zimakov, E.A. Stabilization of the mechanical properties of rolled products after the reconstruction of the laminar cooling system on 1700 Hot Strip Mill. *Metallurg*. **2005**, 2, 42-44 (in Russian).
27. Belobrov, Yu.N.; Gritsenko, S.A.; Eletskih, V.I.; Kozhevnikov, G.V.; Vakulenko, A.M., Ostapenko, A.L., Beygelzimer, E.E., Kuzmin, A.V.; Egorov, N.T. Creation of a modern complex for heat treatment of heavy-plate products at the HSW HUTA STALI metallurgical plant, Poland. *Chernaya metallurgiya. Byull.* **2008**, 8, 36-39 (in Russian).
28. Beygelzimer, E.E.; Ostapenko, A.L.; Kuzmin, A.V.; Kozlenko, D.A. Integrated software for ACS of controlled cooling of rolled sheets. *Stal*. **2006**, 8, 18-23 (in Russian).
29. Ning, J.; Liang, S.Y. Evaluation of an Analytical Model in the Prediction of Machining Temperature of AISI 1045 Steel and AISI 4340 Steel. *J. Manuf. Mater. Process*. **2018**, 2, 74. [https://doi.org/10.3390/jmmp2040074].
30. Shokrani, A., Biermann, D. Advanced Manufacturing and Machining Processes. *J. Manuf. Mater. Process.* **2020**, 4, 102. [https://doi.org/10.3390/jmmp4040102].

31. Beygelzimer, E.E. and Beygelzimer, Y.E. Calculation of the theoretical dimensions of the spray impact spot taking into account the inclination and rotation of the nozzle. *Izvestiya Vuzov. Chernaya Metallurgiya*, **2012**, 8, 32-36 (in Russian).
32. Visaria, M.; Mudawar, I. Theoretical and experimental study of the effects of spray inclination on two-phase spray cooling and critical heat flux. *Int. J. Heat Mass Transf.* **2008**, 51(9-10), 2398–2410. [https://doi.org/10.1016/j.ijheatmasstransfer.2007.08.010]
33. Beygelzimer, E.E.; Beygelzimer, Y.E. Engineering calculation of sprayer jet form for cooling metal sheets. *Izvestiya Vuzov. Chernaya Metallurgiya*, **2012**, 55(6), 43-47 (in Russian). [https://doi.org/10.17073/0368-0797-2012-6-43-47]
34. Idelchik, I.E. *Handbook of Hydraulic Resistance*. 4th ed. Begell House Inc., **2008**, 861 p.
35. Chaudhry, M.H. *Open-Channel Flow*. 2nd ed. Springer, **2008**, 523 p.
36. Munson, B.R.; Young, D.F.; Okiishi, T.H. *Fundamentals of fluid mechanics*. 4th ed. John Wiley & Sons, Inc., **2002**, 928 p.
37. Beygelzimer, E.E. An engineering method for estimation of the radius of a contact-spot, formed by the round liquid jet on the upper surface of hot rolled sheet. *Metal and Casting of Ukraine*, **2011**, 219(8), 12-19 (in Russian).
38. Lord Rayleigh, O.M. On the Theory of Long Waves and Bores. In Proceedings of the Royal Society of London. Series A, Published By Royal Society, **1914**, 619(90), 324-328. [https://www.jstor.org/stable/93519]
39. Watson, E.J. The Spread of the Liquid Jet Over a Horizontal Plane. *J. Fluid Mech.*, **1964**, 20, 481-499 [https://doi.org/10.1017/S0022112064001367]
40. Subramanya, K. *Flow in open channels*. 3rd ed. Tata McGraw-Hill Publishing Co. **2009**, 547 p.
41. Beygelzimer, E.E. About the calculation of the length of the intensive cooling of sheet metal by water curtains. *Metal and Casting of Ukraine*, **2011**, 223(12), 48-54 (in Russian).
42. Beygelzimer, E.E. Engineering method for evaluation of thickness and velocity of the water layer, spreading over the upper surface of the wide strip when jet cooling. *Metal and Casting of Ukraine*, **2012**, 234(11), 21-30 (in Russian).
43. Beygelzimer, E.E. Estimation of length of the water layer, unlimitedly spreading over the upper surface of strip when jet cooling. *Metal and Casting of Ukraine*, **2012**, 235(12), 19-24.
44. Batchelor, G.K. *An Introduction to Fluid Dynamics*. Cambridge, England: Cambridge University Press, **2000**, 615 p.
45. Cheong, H.-F. Discharge Coefficient of Lateral Diversion from Trapeziodal Channel. *J. Irrig. Drain Eng*. **1991**, 117, 461-475. [https://doi.org/10.1061/(ASCE)0733-9437(1991)117:4(461)]
46. Beygelzimer, E. Approach to the simulation of jet-impingement cooling based on the reference points of boiling curve: *Metallurgical and Ore Mining Industry*. **2017**, 5, 85-90 (in Russian).
47. Nukiyama, Sh. The maximum and minimum values of the heat Q transmitted from metal to boiling water under atmospheric pressure: Int. J. Heat Mass Transf., **1984**, 27 (7), 959-970. [https://doi.org/10.1299/jsmemagazine.37.206_367]
48. Kalinin, E.K.; Berlin, I.I., Kostiouk, V.V. Transition Boiling Heat Transfer: In book: *Advances in Heat Transfer*, Vol. 18. Moscow: Academic Press, Inc., **1987**, 241-323. [https://doi.org/10.1016/S0065-2717(08)70120-5]
49. Skripov, V.P.; Pavlov, P.; Sinitsyn, E.N. Heating of liquids to boiling by a pulsating heat supply: 2. Experiments with water, alcohols, n-hexane and nonane. *High Temperature*, **1965**, 3 (5), 670-674.
50. Lykov, A.V. Analytical Heat Diffusion Theory. New York, Academic Press, Inc. **1968**, 685 p.
51. Makovskiy, V.A. Empirical formulas for expressing the temperature dependence of the thermophysical properties of steel. *Steel* 1972, 1, 87-89 (in Russian).
52. Beygelzimer, E. and Beygelzimer, Y. Generalized estimates for the density of oxide scale in the range from 0 °C to 1300 °C, 2021, 9 p. arXiv:2110.09791v1
53. Beygelzimer, E. and Beygelzimer, Y. Thermal conductivity of oxide scale and its components in the range from 0 °C to 1300 °C: Generalized estimates with account for movability of phase transitions, 2021, 9 p. arXiv:2110.11632v1
54. Beygelzimer, E. and Beygelzimer, Y. Generalized estimates for thermal expansion of oxide scale in the range from 0 °C to 1300 °C with account for movability of phase transitions in its components, 2021, 10 p. arXiv:2110.08528v1
55. Beygelzimer, E. and Beygelzimer, Y. Heat Capacity of oxide scale in the range from 0 C to 1300 C: Generalized estimates with account for movability of phase transitions, 2021, 8 p. arXiv:2110.11101v1
56. Kutateladze, S.S.; Styrikovich, M.A. *Hydrodynamics of Gas-Liquid Systems*. Moscow: Energiya, 1976, 296 p. (in Russian).
57. Johnson, H.A. Transient boiling heat transfer to water. *Int. J. Heat Mass Transf.* 1971, 14(1), 67-82. [https://doi.org/10.1016/0017-9310(71)90141-4]
58. Ershov, I.Ya.; Kuvaeva, A.M. Influence of the degree of subcooling on the boiling heat transfer coefficient. *Izvestiya Vuzov. Energetika*. **1962**, 11, 84-87. (in Russian)
59. Wang, B.-X.; Shi, D.-H. A semi-empirical theory for forced-flow turbulent film boiling of subcooled liquid along a horizontal plate. *Int. J. Heat Mass Transf.*, **1985**, 28(8), 1499-1505. [https://doi.org/10.1016/0017-9310(85)90252-2].
60. Kutateladze, S.S. *Fundamentals of heat transfer*. London: Edward Arnold, **1963**, 485 p.
61. Kutateladze, S.S.; Leontev, A.I. *Heat and mass transfer and friction in the turbulent boundary layer*. Moscow: Energoatomizdat, **1985**, 320 p.
62. Isachenko V.P., Kushnyrev V.I. *Jet cooling*. Moscow: Energoatomizdat, **1984**, 216 p. (in Russian).
63. Vander Voort, G.F. (Ed.). *Atlas of Time-Temperature Diagrams for Irons and Steels*. ASM Int., **1991**, 783 p.
64. Popova, L.E.; Popov, A.A. Diagrams of Transformation of Austenite in Steels and of Betta Solution in Titanium Alloys. A Handbook of Heat Treatment Specialist. 3rd ed. Moscow, Metallurgiya, **1991**, 503 p. (in Russian).
65. Callister, Jr., W.D.; Rethwisch, D.G. *Material Science and Engineering: An Introduction*. 8-th ed. John Wiley & Sons, **2010**, 1000 p.

66. Scheil, E. Anlaufzeit der Austenitumwandlung [Start-up time of austenite transformation]. *Archiv Für Das Eisenhüttenwesen*, **1935**, 12(8), 565–567. [https://doi.org/10.1002/srin.193500186]
67. Lusk M., Jou, H.-J. On the Rule of Additivity in Phase Transformation Kinetics. *Metall Mater Trans A*, **1997**, 28A, 287-291. [https://doi.org/10.1007/s11661-997-0131-5]
68. Carlone, G.S.; Palazzo, R.; Pasquino. Finite element analysis of the steel quenching process: Temperature field and solid–solid phase change. *Computers & Mathematics with Applications*, 59(1), **2010**, 585-594. [https://doi.org/10.1016/j.camwa.2009.06.006].
69. Lička, S.; Wozniak, J. Matematický model pro analýzu technologických podmínek válcování ocelí za tepla [Mathematical model for the analysis of technological conditions of hot rolling of steels]. *Hutn Aktl*. VUHZ, **1981**, 22(9), 1–49.
70. Mazur, V.L.; Nogovitsyn, O.V. *Theory and Technology of Sheet Rolling: Numerical Analysis and Applications*. Boca Raton, USA: CRC Press, **2018**, 494 p. [https://doi.org/10.1201/9781351173964]
71. Pereloma, E.; Edmonds, D.V. (eds.) *Phase transformations in steels. Vol.1. Fundamentals and diffusion-controlled transformations*. Oxford, Cambridge, Philadelphia, New Delhi: Woodhead Publ. **2012**, 634 p.
72. Austin, J.B.; Rickett, R.L. Kinetics of the decomposition of austenite at constant temperature. *Trans. Am. Inst. Min. Metall. Eng*. **1939**, 964, 1–20.
73. Starink, M.J. Kinetic equations for diffusion-controlled precipitation reactions. *J. Mater. Sci*. **1997**, 32, 4061— 4070.
74. Koistinen, D.P.; Marburger R.E. A general equation prescribing the extent of the austenite-martensite transformation in pure iron-carbon alloys and plain carbon steels. *Acta Metallurgica*, **1959**, 7, 59-60.
75. Ariza, E.A.; Martorano, M.A.; de Lima, N.B.; Tschiptschin, A.P. Numerical Simulation with Thorough Experimental Validation to Predict the Build-up of Residual Stresses during Quenching of Carbon and Low-Alloy Steels. *ISIJ Int.*, **2014**, 54(6), 1396–1405.
76. Allen III, M.B.; Isaacson, E.I. *Numerical Analysis for Applied Science*. 2nd ed. John Wiley&Sons Inc., **2019**, 583 p.
77. Tiunov, V.N.; Gritsenko, S.A.; Ostapenko, A.L.; Beygelzimer, E.E.; Kozlenko, D.A. PAO NKMZ roller quenching machines. *Steel Transl.* **2014**, 44, 921–925 [https://doi.org/10.3103/S0967091214120171]
78. Ostapenko, A.L.; Goncharov, N.V.; Kuzmin, A.V. et al. Experimental investigations into cooling the sheets and plates in the rolling quenching machine. *Chern. Metall. Bull. Sci. Tech. Econ. Inform.* **2008**, 8, 43-49 (in Russian).
79. Ostapenko, A.L.; Beygelzimer, E.E.; Kozlenko, D.A. et al. Sheet cooling in a roller quenching machine. *Steel Transl*. **2016**, 46, 349–355. [https://doi.org/10.3103/S0967091216050119]
80. Birks, N.; Meier, G.H. *Introduction to high temperature oxidation of metals*. London, GB: Edward Arnold, **1983**; 198 p.
81. Arreola-Villa, S.A.; Vergara-Hernández, H.J.; Solorio-Diáz, G.; Pérez-Alvarado, A.; Vázquez-Gómez, O. and Chávez-Campos, G-M. Kinetic Study of Oxide Growth at High Temperature in Low Carbon Steel. *Metals* **2022**, 12, 147 [https://doi.org/10.3390/met12010147].
82. Kubaschewski, O.; Hopkins, B.E. *Oxidation of Metals and Alloys*, 2nd ed. London, GB: Butterworths Scientific Publications, **1962**, 239 p.
83. Peretyatko, V.N.; Temlyantsev, N.V.; Temlyantsev, M.V.; Mihaylenko, Yu.E. *Heating of steel slabs*. Moscow, Russia: Teplotehnik, **2008**, 192 p. (in Russian).
84. Sun, B.; Cheng, L; Du, Ch.-Y.; Zhang, J.-K.; He, Y.-Q. and Cao, G.-M. Effect of Oxide Scale Microstructure on Atmospheric Corrosion Behavior of Hot Rolled Steel Strip. *Coatings* **2021**, 11, 517. [https://doi.org/10.3390/coatings11050517].
85. Sukov, G.S.; Tiunov, V.N.; Gritsenko S. A. Improving the design of a roller quenching machine for heat treatment of sheet metal. *Chernaya metallurgiya. Byull*. **2016**, 4, 68-74.
86. Beygelzimer, E. Effect of scale on the shape of the boiling curve during jet-impingement cooling: *Metallurgical and Ore Mining Industry*. **2018**, 1, 59-62 (in Russian).
87. Zholkov, Y.A. Thermal inertia of thermocouples. *Meas. Tech*. **1961**, 4, 983–985. [https://doi.org/10.1007/BF00977304]

 doi:10.20944/preprints202206.0249.v1

Appendix A

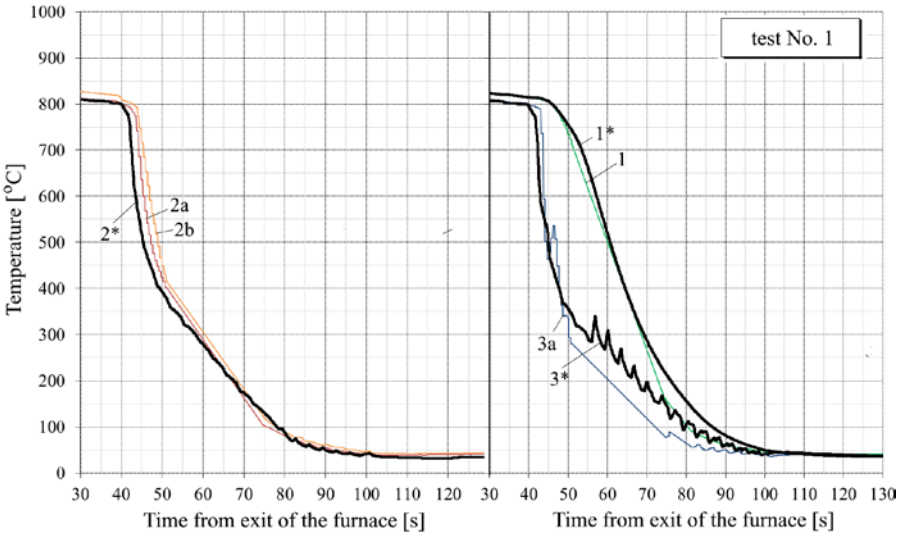

Figure A1. Graphs of cooling in the test No. 1. Numbers without an asterisk denote experimental curves according to the thermocouple data: 1 –at the center of the thickness in the middle of the plate width, 2a - at the top in the middle of the width, 2b - at the top at the edge, 3a - at the bottom in the middle of the width. Numbers with one asterisk indicate calculated curves for the corresponding control points across the thickness of the plate: 1* - at the center of the sheet thickness, 2* - at the depth of 3 mm from the top surface, 3* - at the depth of 2.5 mm from the bottom surface.

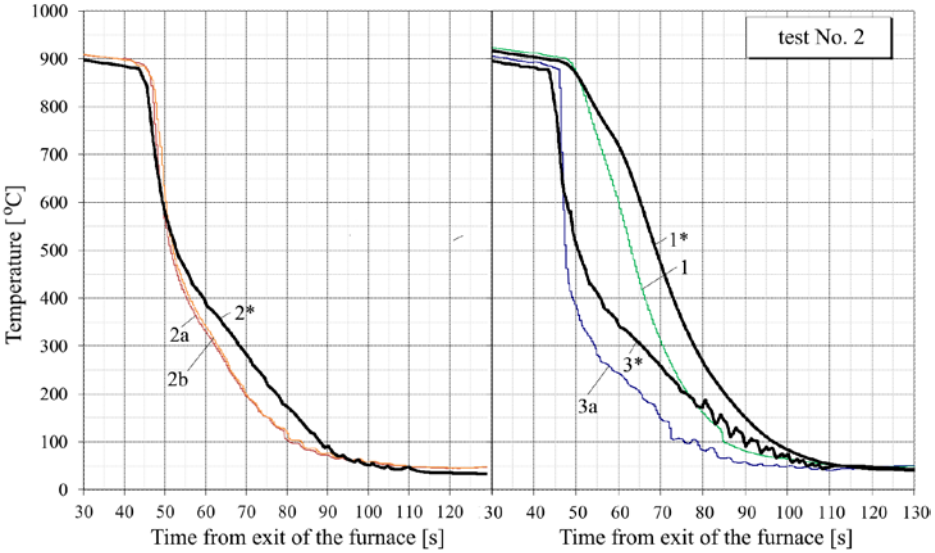

Figure A2. Graphs of cooling in test No. 2. The notations are the same as in Figure A1.

Preprints (www.preprints.org) | NOT PEER-REVIEWED | Posted: 17 June 2022 doi:10.20944/preprints202206.0249.v1

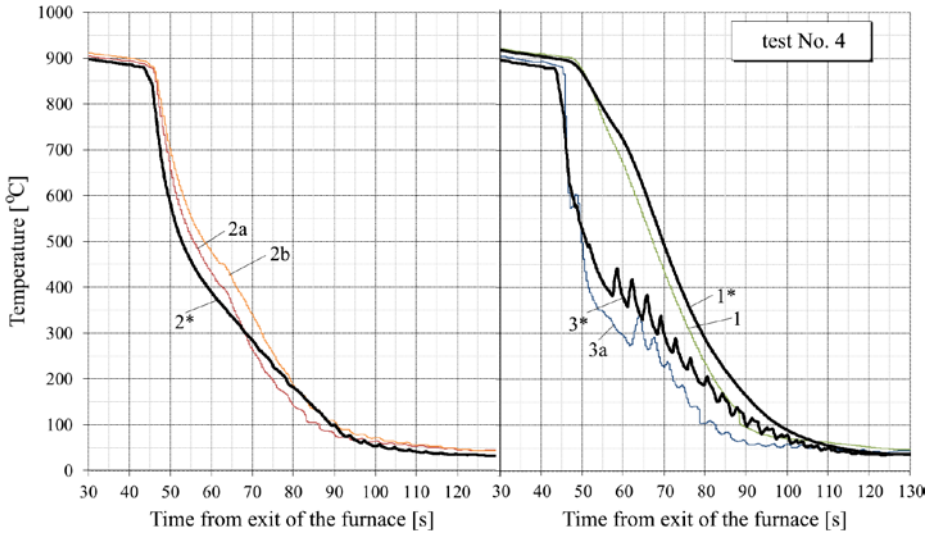

Figure A3. Graphs of cooling in test No. 4. The notations are the same as in Figure A1.

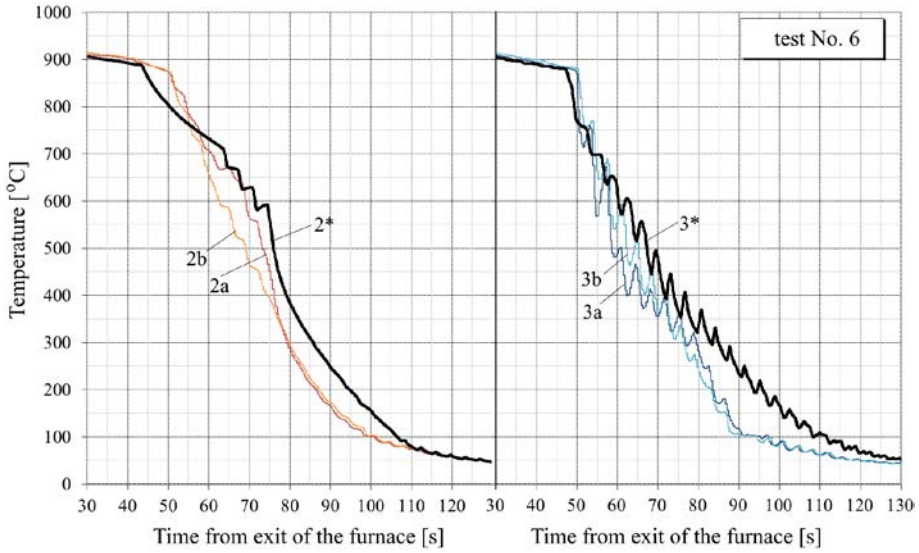

Figure A4. Graphs of cooling in the test No. 6. Numbers without an asterisk denote experimental curves according to the thermocouple data: 2a - at the top in the middle of the width, 2b - at the top at the edge, 3a - at the bottom in the middle of the width, 3b - at the bottom at the edge. Numbers with one asterisk indicate calculated curves for the corresponding control points across the thickness of the plate: 2* - at the depth of 3 mm from the top surface, 3* - at the depth of 2.5 mm from the bottom surface.

Preprints (www.preprints.org) | NOT PEER-REVIEWED | Posted: 17 June 2022 doi:10.20944/preprints202206.0249.v1

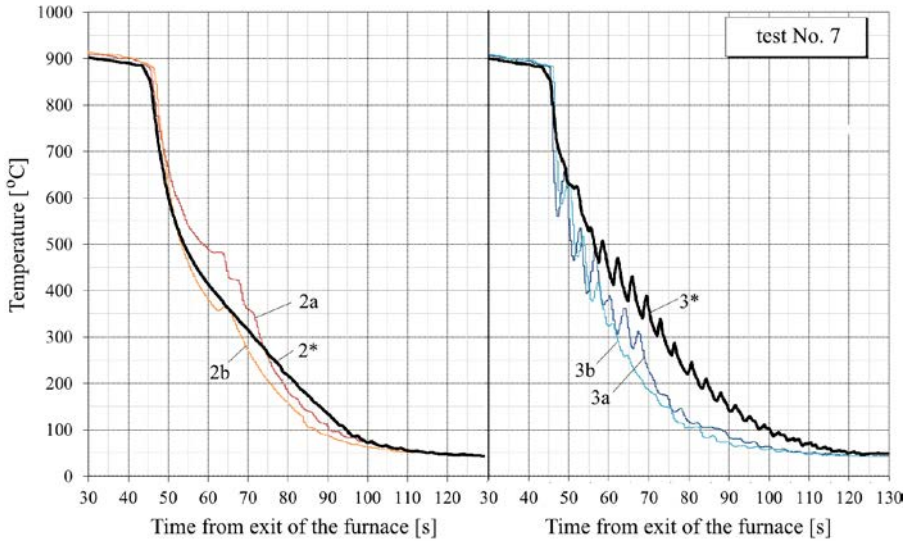

Figure A5. Graphs of cooling in test No. 7. The notations are the same as in Figure A4.

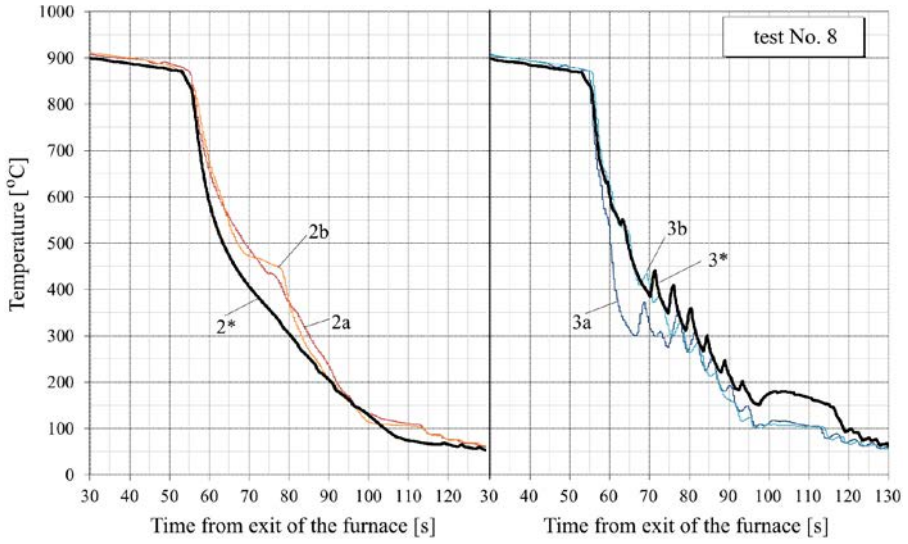

Figure A6. Graphs of cooling in test No. 8. The notations are the same as in Figure A4.

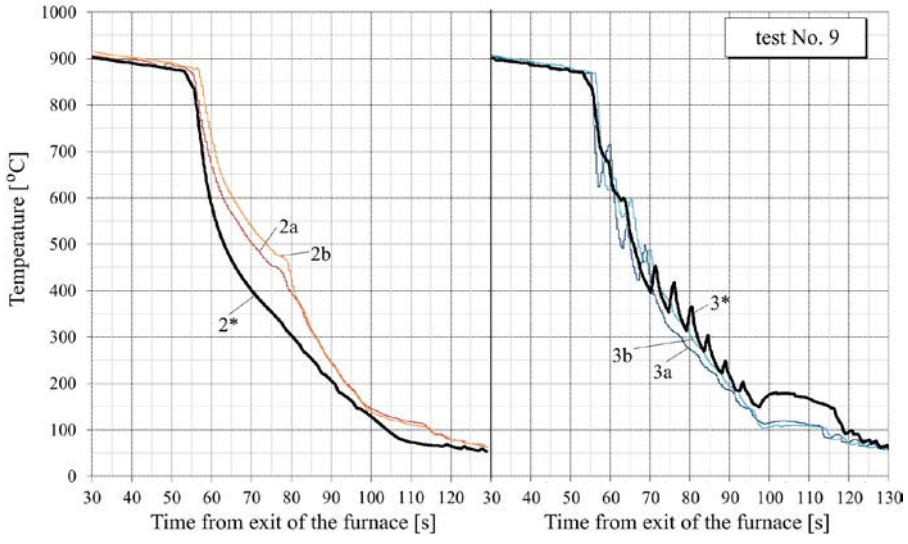

Figure A7. Graphs of cooling in test No. 9. The notations are the same as in Figure A4.